Optimally Distributed Receiver Placements Versus an Environmentally Aware Source: New England Shelf Break Acoustics Signals and Noise Experiment

William K. Stevens, Martin Siderius, Matthew J. Carrier, and Drew Wendeborn

***Abstract*—This article describes the results of the Spring of 2021 New England Shelf Break Acoustics (NESBA) Signals and Noise experiment as they pertain to the optimization of a field of passive receivers versus an environmentally aware source with end-state goals. A discrete optimization has been designed and used to demonstrate providing an acoustic system operator with actionable guidance relating to optimally distributed receiver locations and depths and likely mean source detection times and associated uncertainties as a function of source and receiver levels of environmental awareness. The uncertainties considered here are those due to the imperfect spatial and temporal sensing of the water column, ambient noise (AN), and the seabed, and the impact this has on ocean forecasting and acoustic performance prediction accuracy. As a part of the NESBA experiment, high-resolution (1 km spatial) regional Navy Coastal Ocean Model ensemble forecasts were generated to capture oceanographic variability and uncertainty. Passive AN-based seabed measurements were conducted to estimate seabed properties including variability and uncertainty. Extensive AN and conductivity, temperature, and depth measurements were also conducted. In this article, operationally relevant metrics are employed to estimate the potential value-added of optimal receiver location and depth placements as a function of source end-state goals and assumed level of environmental awareness. A concept for generating stochastic acoustic prediction metrics and associated optimally distributed receiver locations and depths in an operational environment is proposed.**

***Index Terms*—Cumulative probability of detection (CPD), distributed acoustic receiver placement optimization, passive sonar, uncertainty.**

I. Introduction

OCEAN acoustic predictions, especially in littoral regions, are subject to large uncertainties due to both ocean statistical fluctuations [1], [2], [3] and uncertainties in key model parameters relating to oceanography [four-dimensional (4-D) sound speed profiles (SSPs)], the seabed, and ambient noise (AN). Despite this fact, ocean acoustic predictions are not generally presented to acoustic system operators with uncertainty bounds [4], [5], [6].

Transmission loss (TL) modeling is complicated by acoustic propagation conditions that are driven by temporal and spatial variations and uncertainties in ocean surface conditions (winds and waves), water column variations with depth (temperature and salinity), bathymetry, and complex seabed characteristics [6], [7]. In the New England Shelf Break Acoustics (NESBA) experiment area, the proximity of the Gulf Stream results in eddy formation and frontal position changes that can dramatically alter local sound speeds versus depth and range. Seabed variations from the continental shelf to slope to deeper plateau regions can also be significant. Uncertainties in water column and seabed properties can be reduced using in situ onboard and offboard measurement systems. Nevertheless, TL variability and uncertainty can, and often do, result in significant mismatch between deterministic sonar performance predictions and at-sea measurements and real-world sonar performance.

Similarly, AN modeling [8] is complicated by the characteristics of noise due to wind, wave action, rain, biologics, and shipping as a function of time, direction, and location over a broad range of tactical frequencies. This is again especially true in the NESBA experiment area due to high levels of shipping and fishing activity and the proximity of the Gulf Stream. Sonar system planning ashore typically employs Wentz curve data [9] or other AN databases [10] to estimate likely AN values, leading often to substantial mismatches between planned and actual sonar system performance. Once in situ, however, onboard or offboard AN measurements can be used to reduce AN estimation errors. Nevertheless, as with TL, AN variability and uncertainty can result in a substantial mismatch between deterministic sonar performance predictions and at-sea measurements and real-world sonar performance.

In addition to the inherent uncertainties in the estimation of mean TL and AN levels, random statistical fluctuations in received signal are known to exist due to moving inhomogeneities in the sea caused by source and receiver motion, surface and internal waves, etc. [1], [2], [3]. These fluctuations are especially pronounced for narrowband signals, causing spurious or erratic sonar detections [1], [2].

This article addresses the degree to which the improved ocean environmental awareness demonstrated in the NESBA

Manuscript received 28 October 2022; revised 21 March 2023 and 9 July 2023; accepted 28 July 2023. This work was supported by the Office of Naval Research Task Force Ocean Program under Grant N00014-19-1-2720. *(Corresponding author: William K. Stevens.)*

Associate Editor: Z.-H. Michalopoulou.

William K. Stevens, Martin Siderius, and Drew Wendeborn are with the Department of Electrical and Computer Engineering, Portland State University, Portland, OR 97201 USA, and also with Metron, Inc., Portland, OR 97201 USA (e-mail: wks3@pdx.edu; siderius@pdx.edu; dwendeborn@pdx.edu).

Matthew J. Carrier is with Code 7321: Ocean Data Assimilation and Probabilistic Prediction Branch, U.S. Naval Research Laboratory, Stennis Space Center, MS 39529 USA (e-mail: matthew.carrier@nrlssc.navy.mil).

Digital Object Identifier 10.1109/JOE.2023.3302915

experiment [11] could lead to improved passive sonar source detection and localization performance. A simplified problem is considered in which a source is detected with spatial uncertainty at time zero, the source is known to have the end-state goal of transiting to any one of a collection of known locations as quickly as possible while minimizing its probability of counter-detection, and the sonar operator's goal is to passively redetect and localize the source as quickly as possible. Both the source and the sonar operator are assumed to have known degrees of ocean environmental awareness pertaining to oceanography (range-dependent temperature and salinity versus depth), AN, and seabed characteristics. The objective of this article is to assess the extent to which the advanced environmental sensing and ocean modeling initiatives explored as a part of the 2021 NESBA Signals and Noise experiment could be successfully leveraged in support of this simple operational problem, with the expectation that the methods described herein are likely applicable to more complex operational problems.

Cold War era approaches to this problem [12], [13] were developed for deep water ocean areas in which a single median detection range (MDR) could plausibly be assumed to represent the acoustics for the full search area of interest. In such an area, this MDR could be employed to determine an optimal distributed receiver field with uniform spacings (typically equal to some multiple of MDR) and depth. In shallow or littoral water areas, however, this assumption of MDR uniformity is typically invalid and hence distributed receiver fields with uniform spacing and depths are likely to be substantially suboptimal. In the NESBA experiment area, for instance, the acoustic conditions are strongly nonuniform due to high levels of shipping and fishing activity resulting in highly variable and directional AN, the presence of the Gulf Stream resulting in eddy formation and frontal position changes, and complex seabed characteristics given that the NESBA area spans the continental shelf, slope, and deeper ocean plateau areas. The work described here could provide the basis for a new class of acoustic operator decision support tools capable of exploiting environmental sensing and high-resolution ocean modeling with ensembles for the purpose of generating optimal distributed passive receiver placement locations and depths.

While this article focuses on the optimization of a distributed field of passive receivers, the proposed methodology for leveraging NESBA like environmental forecast data and measurements is not limited to this case. We anticipate that the approach proposed here could be leveraged in support of the optimal employment of bistatic, multistatic [14], [15], [16], or other distributed sensor fields.

II. NESBA Signals and Noise Experiment

In this section, we describe the NESBA Signals and Noise experiment along with the ocean modeling and data postanalysis approaches used to calculate seabed properties and uncertainties, TL and AN mean levels and uncertainties, and signal excess (SE) fluctuation statistics.

A. NESBA Signals and Noise Experiment

The NESBA Signals and Noise experiment was conducted in April–May 2021 as a collaboration between Woods Hole Oceanographic Institute and Portland State University. The goal of the experiment was to assess the potential for sonar prediction effectiveness gain given improved environmental awareness. This article addresses the NESBA subgoal of demonstrating the degree to which high-resolution regional Navy Coastal Ocean Model (NCOM) ocean modeling with ensemble forecasts and enhanced environmental sensing could be leveraged to enable the optimization of a field of passive receivers versus an environmentally aware source with end-state goals.

During NESBA, AN data were collected using four drifting vertical line arrays (VLAs) launched from the R/V *Endeavor* and deployed on a buoyancy engine, each with a hover depth of 10–20 m from the seabed, in three separate deployments as described in Table I. Each VLA was composed of 16 hydrophone elements with 1-m spacing recording at a 10-kHz sample rate. The three survey regions are pictured in Fig. 1.

Conductivity, temperature, and depth (CTD) profiles were collected from the R/V *Endeavor* using a Sea Bird Electronics SBE 911+ CTD and processed using Seasoft software. A CTD profile was collected immediately prior to deployment of each VLA and again after each VLA was recovered. During the array deployment periods, CTD profiles also were collected along transects in the vicinity of the drifting arrays.

During the first two array deployments, only AN data was collected. In the final deployment, NUWC J-15 and ITC 1007 acoustic sources were towed in the vicinity of the drifting arrays. The J-15 source transmitted a series of tones at 53, 97, 147, and 223 Hz and then a linear frequency modulated (LFM) signal from 50 to 1000 Hz. The ITC 1007 source transmitted a 2–4-kHz LFM followed by a 2–4 kHz m-sequence signal, both with 1-s durations.

Additional CTD data were collected from the R/V *Armstrong*, R/V *Sharp*, and Ocean Observatories Initiative fixed moorings in the area, as summarized in Table II. The R/V *Sharp* also towed a profiling Scanfish instrument collecting CTD data along 13 transects. These CTD and Scanfish data collections were conducted over the full duration of the NESBA experiment. Table II summarizes all CTD data collected during NESBA.

Fig. 2 shows a snapshot of NESBA area sea surface temperature (SST) during the time-period of the experiment. The left panel shows SST on May 21, 2021 at 0900 Greenwich Mean Time (GMT) based on the Jet Propulsion Laboratory (JPL) daily merged, multisensor, multiscale, ultrahigh resolution (MUR) SST product. The right panel shows SST based on one NCOM ensemble forecast for the same day and time. The JPL SST data shows the Gulf Stream to the south and the formation of a warm core eddy to the west of the NESBA experiment area. It also shows some warm water incursions into the southern portion of the experiment area. The NCOM ensemble has similar features for this specific ensemble; other NCOM ensembles have similar levels of agreement with the JPL data.

TABLE I
NESBA AN DATA COLLECTIONS

Deployment	Recovery	Duration (Days)	Region
April 25,2021 13:09	April 27, 2021 17:43	2.19	North
April 28,2021 17:30	May 03, 2021 15:52	4.93	Southwest
May 06, 2021 13:50	May 13, 2021 14:34	7.03	Southeast

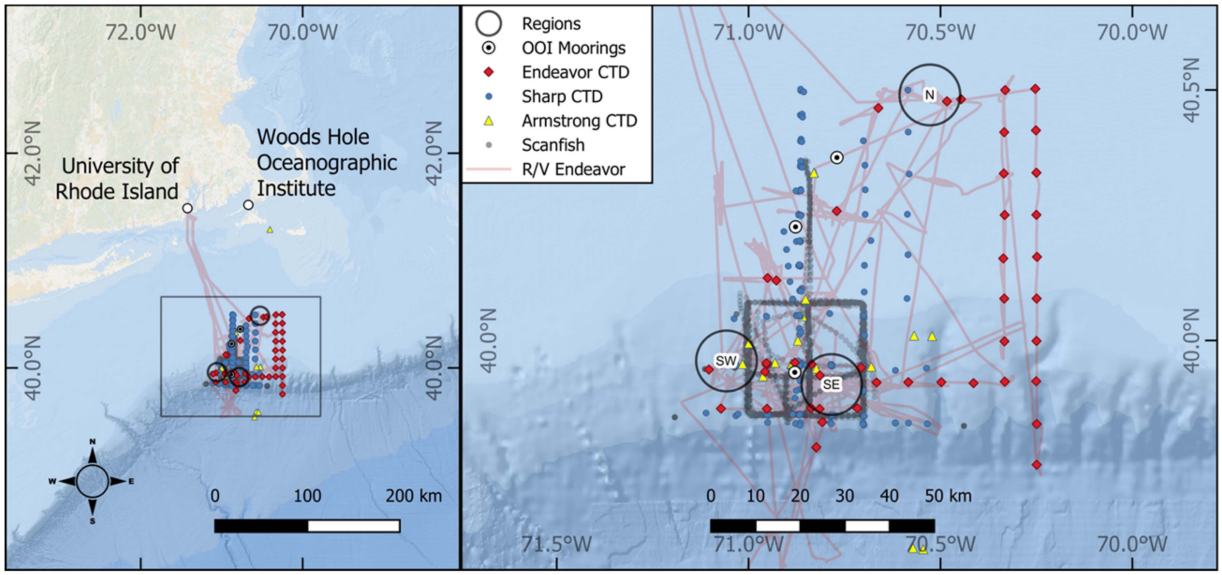

Fig. 1. NESBA Signals and Noise experiment area with North, Southwest, and Southeast survey locations.

TABLE II
CTD DATA COLLECTIONS

Asset	Instrument	CTD profiles
R/V Endeavor	SBE 911+ CTD	54
R/V Sharp	SBE 911+ CTD	129
R/V Armstrong	SBE 911+ CTD	26
CP040SPM	Sea-Bird - SBE 52MP	152
CP02PMCI	Sea-Bird - SBE 52MP	919
CP02PMUI	Sea-Bird - SBE 52MP	560
Scanfish MkII	SBE 911+ CTD	13 transects

B. NCOM Ensemble Forecasts

The NCOM is an operational U.S. Navy regional ocean model. During NESBA, 50 NCOM 96-h ensemble forecasts were generated daily in the roughly 6° × 6° region just south of the New England coast from 73.0° W to 67.0° W longitude and 37.0° N to 42.5° N latitude (see Fig. 3). These runs were conducted with 1 km horizontal resolution and 50 vertical levels (25 bathymetry following levels and 25 constant depth levels) extending past 4500 m depth in the deepest part of the domain. Standard observation sources assimilated included satellite SST from the Geostationary Operational Environmental Satellite (GOES) 16, Meteorological Operational Satellite (METOP), Visible Infrared Imaging Radiometer Suite (VIIRS), and ocean-bound ship observations and NOAA buoys; satellite sea surface height anomaly (SSHA) from JASON-3, Sentinel-3A, Sentinel-3B, and SARAL/AltiKa DP; and ocean temperature and salinity profiles from the ARGO program. The NCOM forecasts generated during the NESBA experiment are referred to in this article as the *NCOM baseline forecasts*.

After the conclusion of the NESBA experiment, an NCOM ensemble reanalysis was conducted for the full NESBA timeframe with the added assimilation of all water-column measurements described above in Section II-A. The NCOM forecasts generated post-NESBA are referred to in this article as the *NCOM nature reanalysis*.

See the Appendix for a more detailed description of these NCOM ocean model ensemble runs.

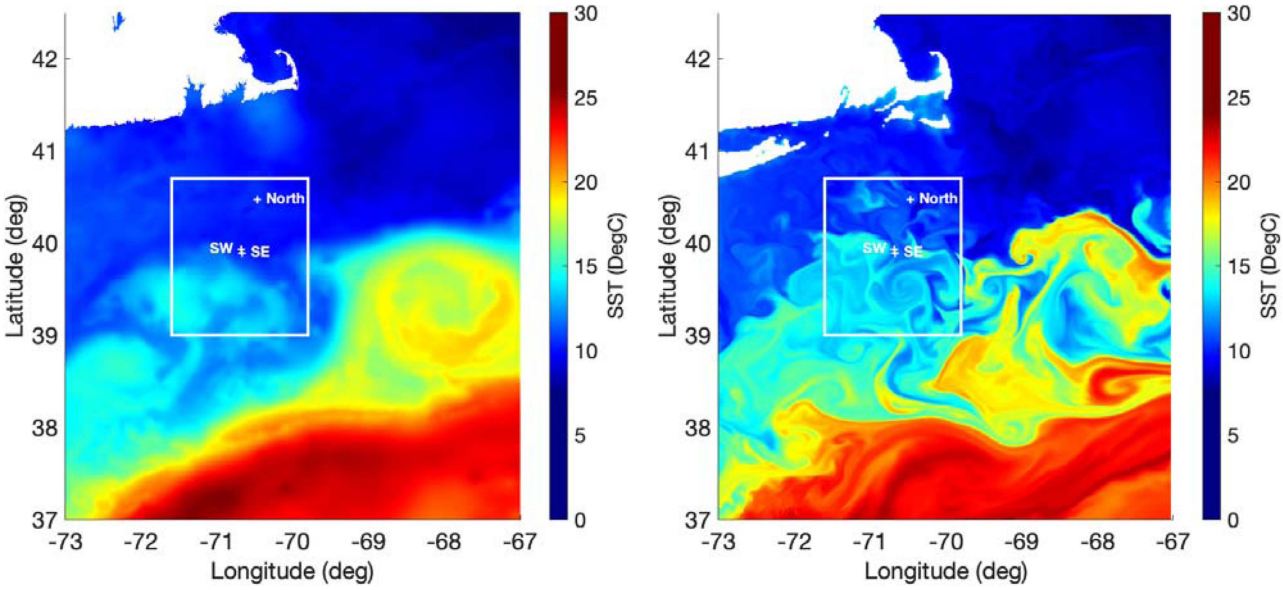

Fig. 2. NESBA area SST on May 21, 2021, 0900 GMT. Left: SST based on JPL MUR product. Right: SST based on one NCOM ensemble forecast.

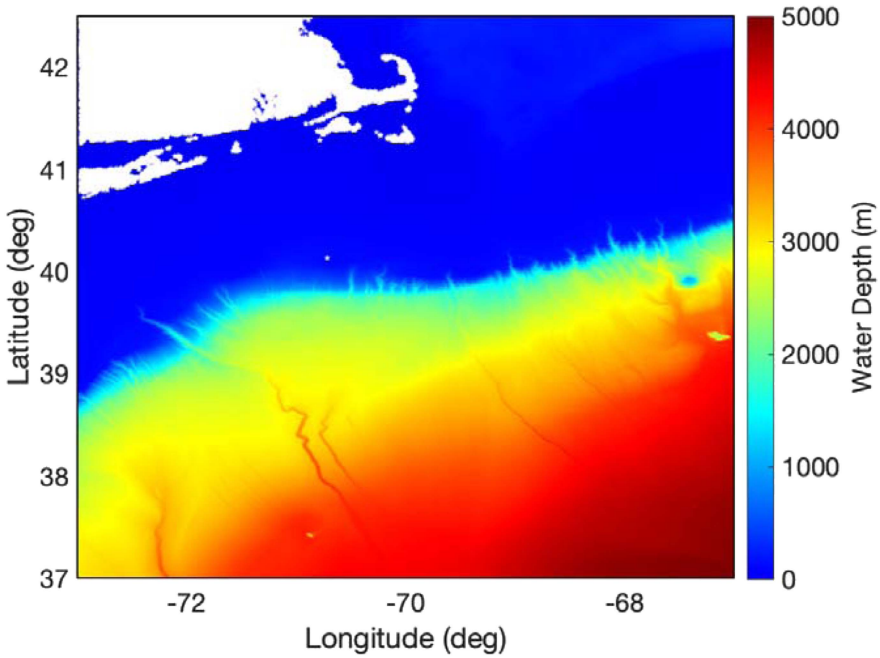

Fig. 3. NCOM domain used for modeling experiments. Color contours indicate ocean bathymetry in meters based on the General Bathymetric Chart of the Ocean (GEBCO) [18].

NCOM ensemble forecasts are used here as the means to capture oceanographic uncertainty under the supposition that the 50 NCOM ensemble forecasts generated as described in the Appendix provide a capture of the span of likely true ocean states. In addition, the NCOM nature ensemble mean reanalysis is assumed to be the best capture of the true ocean state. This NCOM reanalysis is used here as the "nature" environment, i.e., it is used as the best estimate of the true ocean state consistent with what is typically referred to as an Observing System Simulation Experiment [17] analysis approach.

C. Noise-Based Seabed Mean and Uncertainty Estimation

Seabed properties and their uncertainties are needed to estimate TL and TL uncertainty levels. TL models typically are based upon seabed parameters such as sound speed, attenuation, and density. During the NESBA experiment, bottom loss measurements were conducted using a technique based on wind-driven ambient sound [19]. This method, commonly referred to as R-θ (as in reflection loss versus angle), is a relatively simple method that only requires beamforming

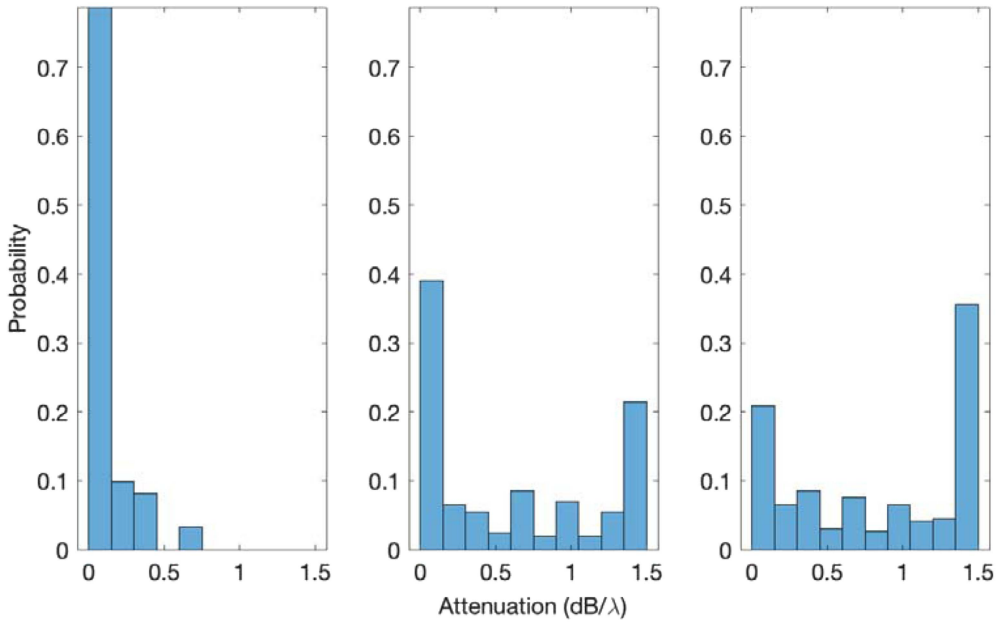

Fig. 4. Measured seabed attenuation probability distributions. Left: North survey area. Middle: Southeast survey area. Right: Southwest survey area.

surface generated noise primarily from wind and received on a vertical hydrophone array. In the NESBA experiment, four 16-hydrophone VLAs with 1 m element spacing were deployed in three separate locations denoted as the North, Southwest, and Southeast sites in Table I. The arrays drifted in water depths that varied from approximately 70–500 m. The arrays were self-recording with a sampling frequency of 10 kHz and all analysis was done at two frequencies of 250 and 625 Hz. The minimum mean squared error (MMSE) was taken for the sum of the results at the two frequencies. During the experiment, the wind speed varied from 0 to 20 m/s and therefore the surface wave noise also changed during the experiment. The data used here were chosen during periods with sustained wind speeds > 10 m/s. The data processing consisted of dividing the time series data into nonoverlapping snapshots of length 0.4096 s and transforming to the frequency domain using a 4096-sample length fast Fourier transform (FFT). The data snapshots were averaged for 1 min.

Once the data covariance matrix was computed, these data were beamformed and the power reflection loss and bottom loss were estimated. Each beamformed minute of data was compared against modeled data spanning a state space of seabed sound speed, attenuation, and density parameters. The parameters that corresponded to the MMSE for each realization were saved and results from all realizations were combined to produce a mean value.

The result of this passive, noise-based seabed characterization processing is shown in Figs. 4–6 for each of the three estimated seabed parameters. These plots show seabed parameter probability density functions (PDFs) in the North survey area, which is centered on [40.49N,–70.53W] (left panel), the Southeast survey area centered on [39.95N,–71.05W] (middle panel), and the Southwest survey area centered on [39.91N,–70.78W] (right panel).

It should be noted here that, for simplicity, this three-parameter seabed model was used with the goal of representing the main features of the seabed bottom loss curve. This is meant to capture an effective seabed for the frequencies under consideration and is not a detailed geo-acoustic model that might be applicable over a wider band of frequencies.

D. TL Mean and Uncertainty Estimation

TL mean and standard deviation versus range, due to uncertainties in oceanography, the seabed, and combined oceanography plus seabed, have been computed using the Range-dependent acoustic model (RAM) [20], [21]. These TL calculations have been conducted at the geographic centers of the three survey locations listed in Table I. At each survey location, TL calculations were performed along the eight radials ranging from 45° to 360° in steps of 45°.

Range-dependent SSPs were extracted from the NESBA NCOM ensemble forecasts discussed in Section II-B. Each GMT 00 ensemble forecast (having 96-h duration in 3-h time steps) represents one possible ocean state realization for the times and locations of interest. Collectively, the full set of NCOM ensemble forecasts represents a likely range of forecast ocean states given expected uncertainties in NCOM initial conditions and model approximations. Accordingly, NCOM ensembles are used here to estimate TL mean and uncertainty versus range due to uncertainties in oceanography. Fig. 7 shows TL uncertainty versus range (left column) and associated TL mean and standard deviation versus range (right column) due to oceanographic uncertainties in the Southwest survey area for source depth = 25 m, source frequency = 250 Hz, and four receiver depths (30, 60, 120, and 300 m). The horizontal red line in each of these plots is FOM = SL – AN + DI – RD, where SL = source level (assumed here to be 150 dB),

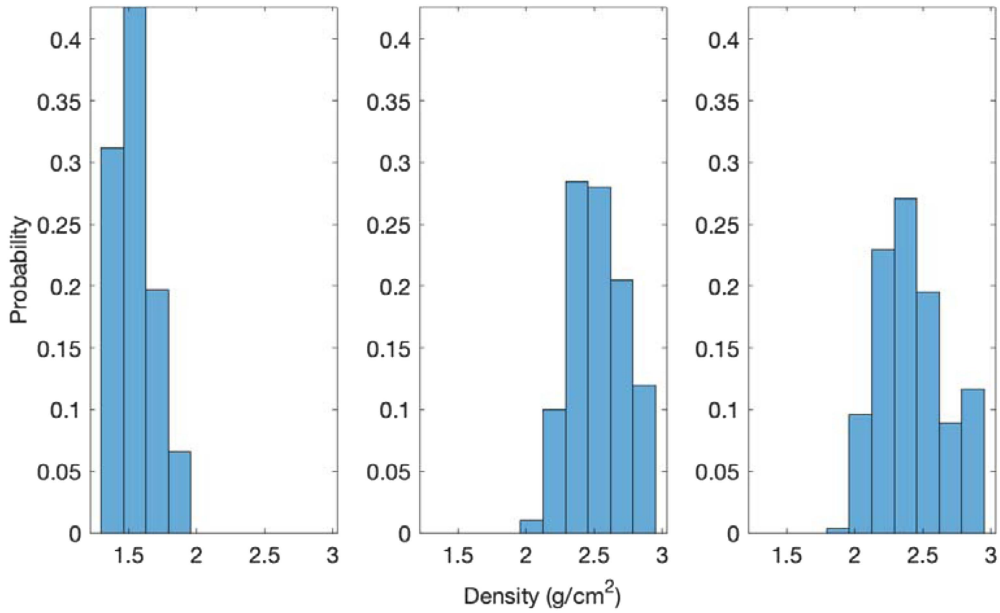

Fig. 5. Measured seabed density probability distributions. Left: North survey area. Middle: Southeast survey area. Right: Southwest survey area.

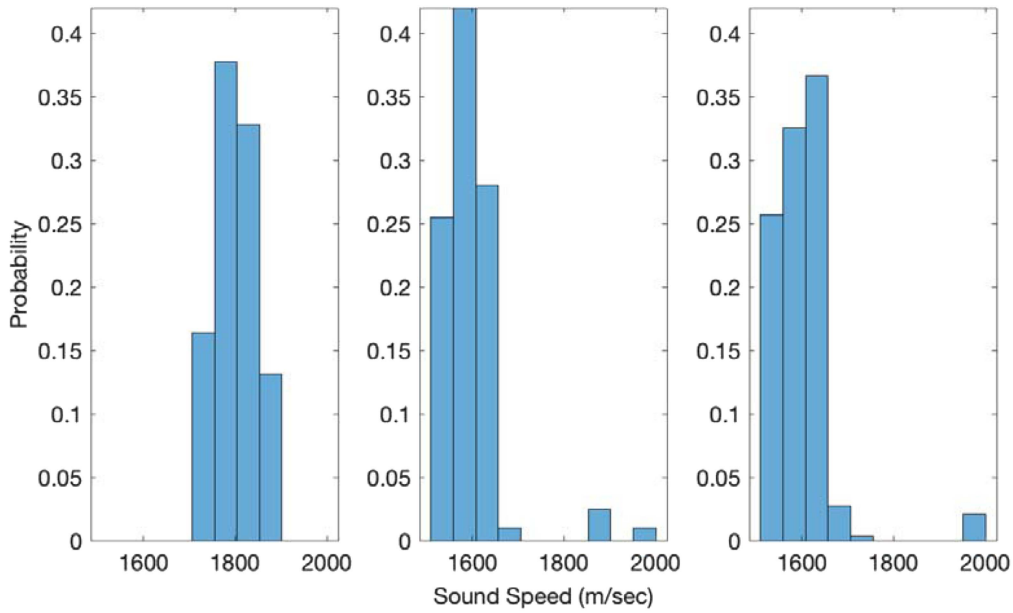

Fig. 6. Measured seabed sound speed probability distributions. Left: North survey area. Middle: Southeast survey area. Right: Southwest survey area.

AN = mean measured omnidirectional AN in the Southwest survey area, DI = directivity index, and RD = recognition differential. DI and RD are both set to nominal values of 0 dB. This same information has been computed for all three survey areas and all relevant source and receiver depths.

Similarly, NESBA AN-based seabed measurements, as discussed in Section II-C, are used to derive likely seabed density, attenuation, and sound speed distributions in relevant NESBA shelf and slope experimentation areas. These distributions in seabed parameters are used to estimate TL versus range mean and uncertainty due to uncertainties and variations in seabed composition. Ocean bathymetry is represented using the GEBCO gridded bathymetric data set [18]. Fig. 8 shows TL uncertainty versus range (left column) and associated TL mean and standard deviation versus range (right column) due to seabed uncertainties in the Southwest survey area for source depth = 25 m, source frequency = 250 Hz, and four receiver depths (30, 60, 120, and 300 m) where again each row corresponds to one receiver depth. This same information has been computed for all survey areas and selected source and receiver depths.

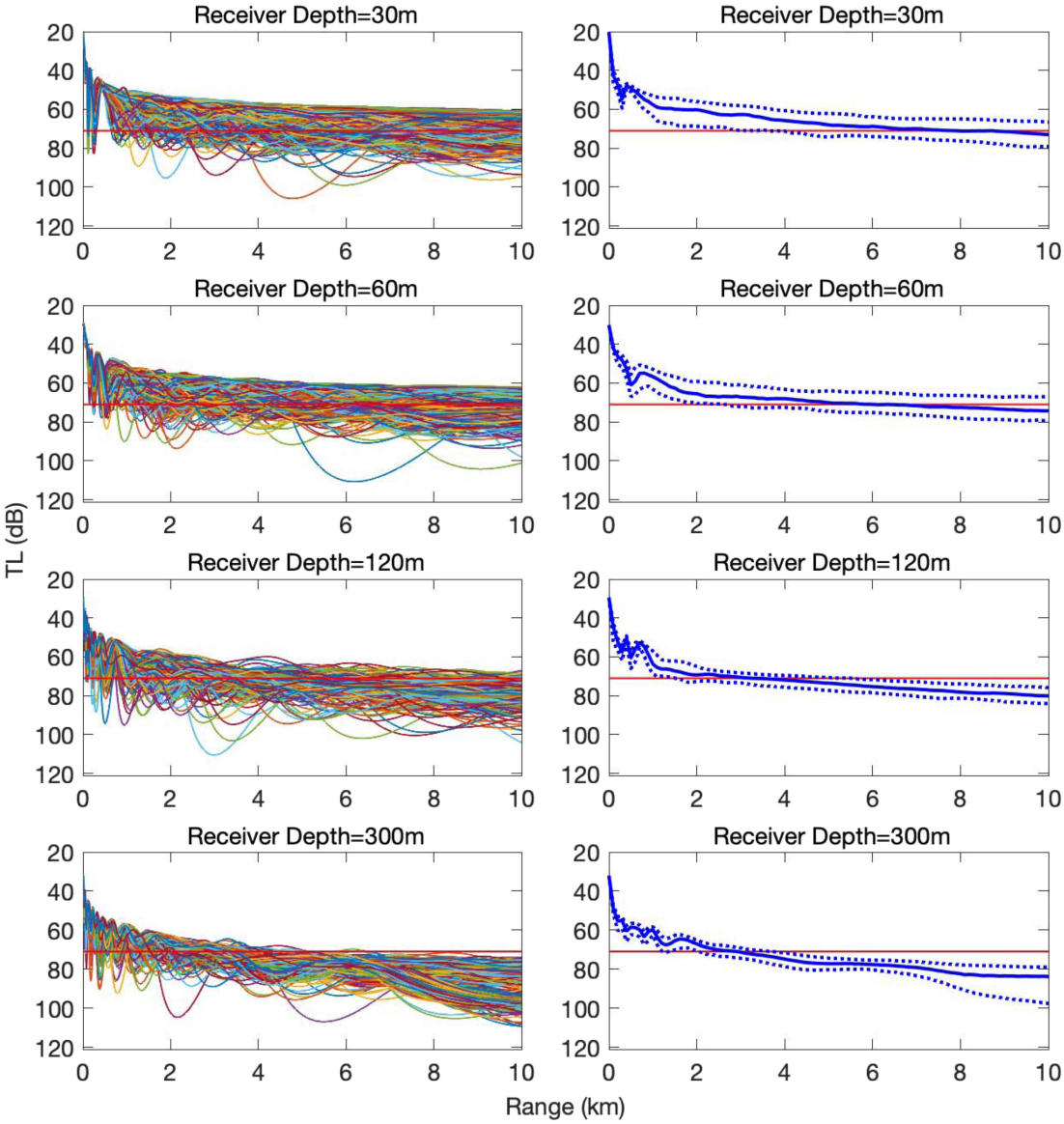

Fig. 7. Example TL sensitivity to oceanographic uncertainty at the Southwest survey area center location for source depth = 25 m, source frequency = 250 Hz, and eight radials. The horizontal red line in each plot is the estimated local figure of merit (FOM). Left column: TL uncertainty versus range. Right column: TL mean (solid blue line) and standard deviation (dashed blue lines) versus range. Rows: Receiver depths = 30, 60, 120, and 300 m.

Finally, the mean and uncertainty of TL versus range due to combined uncertainties in oceanography and seabed parameters are computed using RAM and the combined effects of NCOM ensemble forecasts and seabed parameter PDFs as illustrated in Fig. 9. This same information has been computed for all survey areas and selected source and receiver depths.

E. AN Mean and Uncertainty Estimation

Ocean AN data were collected using four drifting, VLAs hovering less than 50 m above the seafloor at three survey locations during the experiment. A series of 1-min duration recordings were converted to micropascals and the average signal was calculated across all hydrophone elements. The power spectral density (PSD) from 50 to 500 Hz was calculated using Welch's method at 1 Hz bin spacing for each recording. Using the magnitude of the PSDs, the mean and standard deviation at each frequency bin were reported for each of the three experiment locations. These AN measurements are used here to capture AN mean and uncertainty at the three survey locations and survey times in the NESBA experiment area.

The result of the AN data processing described above is shown in Figs. 10–12 for each of the three survey locations. These plots show measured AN mean and standard deviation versus frequency for frequencies in the range of 50–500 Hz (left panel) and the AN power distribution in the 250-Hz band (right panel).

Note that despite the likely importance of AN directionality and time dependence in and around the NESBA experiment site, given its proximity to commercial shipping lanes and fishing activity, it was outside the scope of the NESBA experiment to measure anything beyond omnidirectional AN with

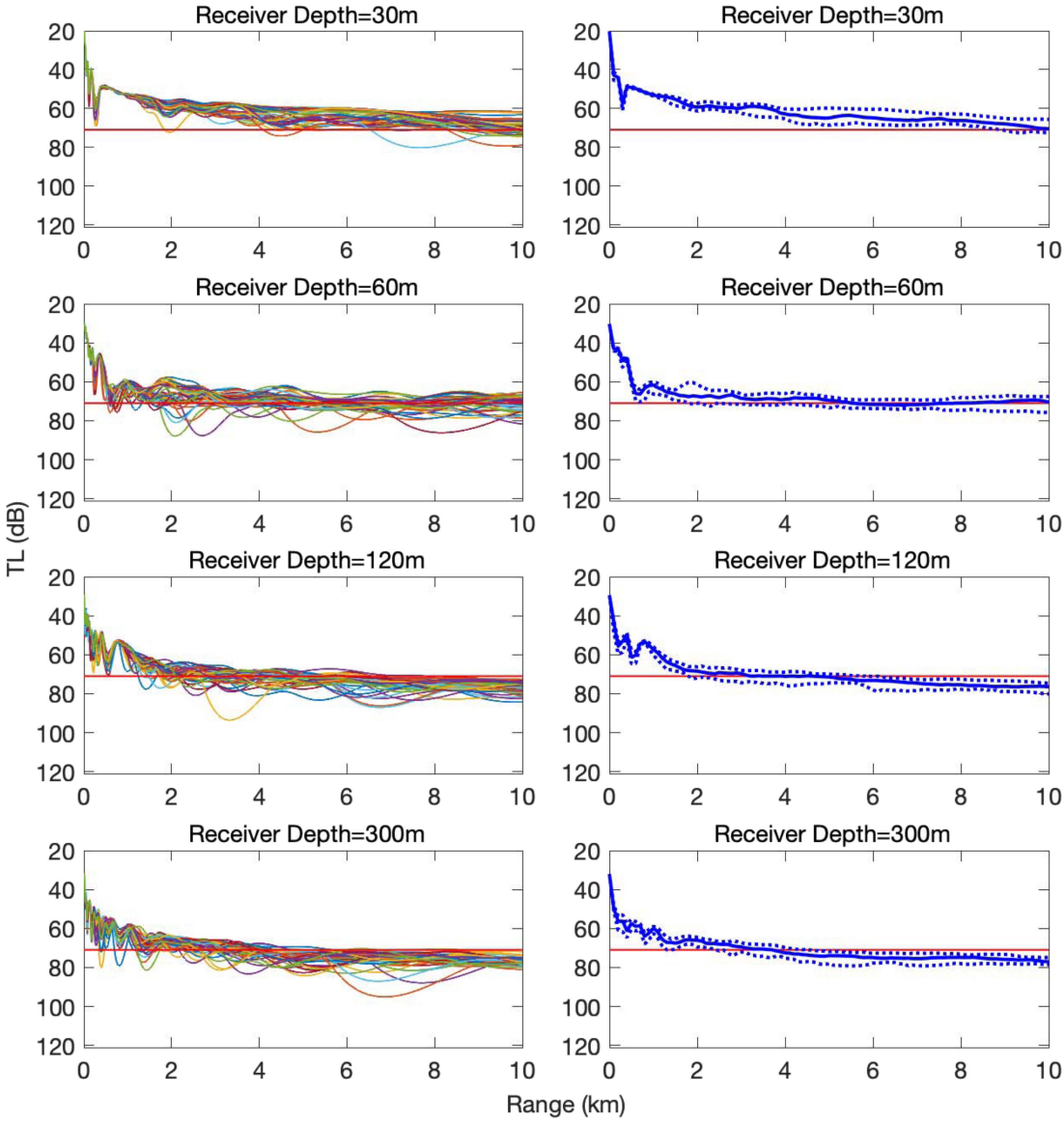

Fig. 8. Example TL sensitivity to seabed uncertainty in the Southwest survey area for source depth = 25 m and source frequency = 250 Hz. The horizontal red line in each plot is the estimated local FOM. Left column: TL uncertainty versus range. Right column: TL mean and standard deviation versus range. Rows: Receiver depths = 30, 60, 120, and 300 m.

uncertainties over a few days duration at each of the three survey areas. A substantially greater data collection effort would have been required to adequately capture the NESBA area directional AN statistics.

F. SE Fluctuation Statistics

Measured TL taken at a single frequency is known to fluctuate in time due to a variety of factors including source–receiver motion, oceanography (e.g., internal waves), scattering, and changes in the background noise. These fluctuations play an important role in detection. Although somewhat counter-intuitive, fluctuations can actually improve detection performance in many cases [1], [2], [3]. If the signal, in the absence of fluctuations, is below a detection threshold, then adding the fluctuations can at times randomly enhance the signal causing it to exceed the threshold and yield a detection. In the absence of these fluctuations, if one assumes a monotonic TL, the cumulative probability of detection (CPD) would look like a step function. This simply means that beyond a certain range, the signal is below the detection threshold and is never detected and for closer ranges, the detection threshold is exceeded and the signal is always detected. This type of step function detection behavior is unrealistic in practice. The fluctuations create extra detection opportunities and cause this transition to be more of a smoothed version of a step function with the amount of smoothing dependent on the specifics of the fluctuations. Therefore, a model of signal fluctuations is needed to determine how an associated CPD curve transitions away from step-like.

In general, it is difficult to measure and quantify the individual factors that contribute to TL fluctuations. Further, even if one were to carefully measure fluctuations, these could vary

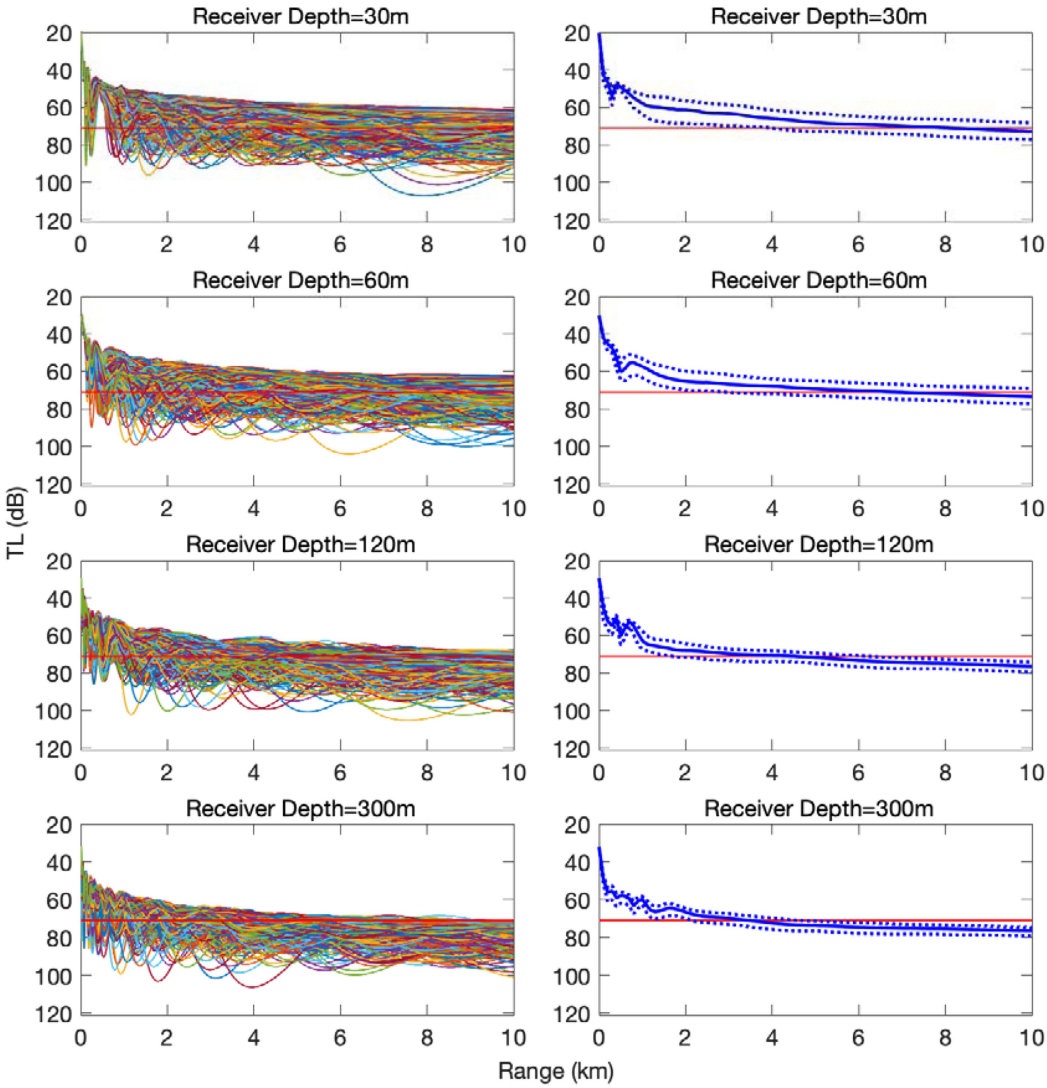

Fig. 9. Example TL sensitivity to combined effects of seabed and oceanographic uncertainty in the Southwest survey area for source depth = 25 m and source frequency = 250Hz. The horizontal red line in each plot is the estimated local FOM. Left column: TL uncertainty versus range. Right column: TL mean (solid blue line) and standard deviation (dashed blue lines) versus range. Rows: Receiver depths = 30, 60, 120, and 300 m.

depending on local conditions at a specific time. In the absence of measurements, what is needed for this analysis is a reasonable model that can be considered typical. Here, the statistics of the fluctuations are taken based on the work of Dyer [2]. In this analysis, using the Dyer notation, the pressure field time series at a single frequency ω is made up of a sum of N multipath signals each with amplitudes A_n and phase ϕ_n given by

$$p\ (t) = \sqrt{\frac{2}{N}}\,\tau \sum_{n\,=\,1}^{N} A_n \cos\left(\omega t - \phi_n\right) \tag{1}$$

with τ accounting for the mean TL such that the amplitudes A_n can be modeled with Gaussian distributed statistics with zero mean and standard deviation of one. The phase ϕ_n is assumed to be uniformly distributed between $0 - 2\pi$.

For the cases considered here, it is reasonable to assume this type of multipath environment with source–receiver motion as well as internal waves and potentially scattering leading to the statistical representations for A_n and ϕ_n. The frequency domain pressure field $p(\omega)$ is estimated using a short time Fourier transform (e.g., STFT). Further, as in [2], it is assumed that the amplitudes and phase are stationary over a short averaging time needed to transform the time domain $p(t)$ to the frequency domain. The short-time-averaged magnitude-squared pressure $\langle |p(\omega)|^2 \rangle_{\text{s.t.av.}}$ can be written as

$$\left\langle |p\,(\omega)|^2 \right\rangle_{\text{s.t.av.}} = \tau^2 \left[\left(\sum_{n\,=\,1}^{N} A_n \cos\phi_n \right)^2 + \left(\sum_{n\,=\,1}^{N} A_n \sin\phi_n \right)^2 \right] \tag{2}$$

where the $\langle \cdot \rangle$ brackets and subscript s.t.av. are used to indicate the short time average. The TL is then given by

$$TL\ (\omega) = -10\log_{10}\left\langle |p\,(\omega)|^2 \right\rangle_{\text{s.t.av.}}. \tag{3}$$

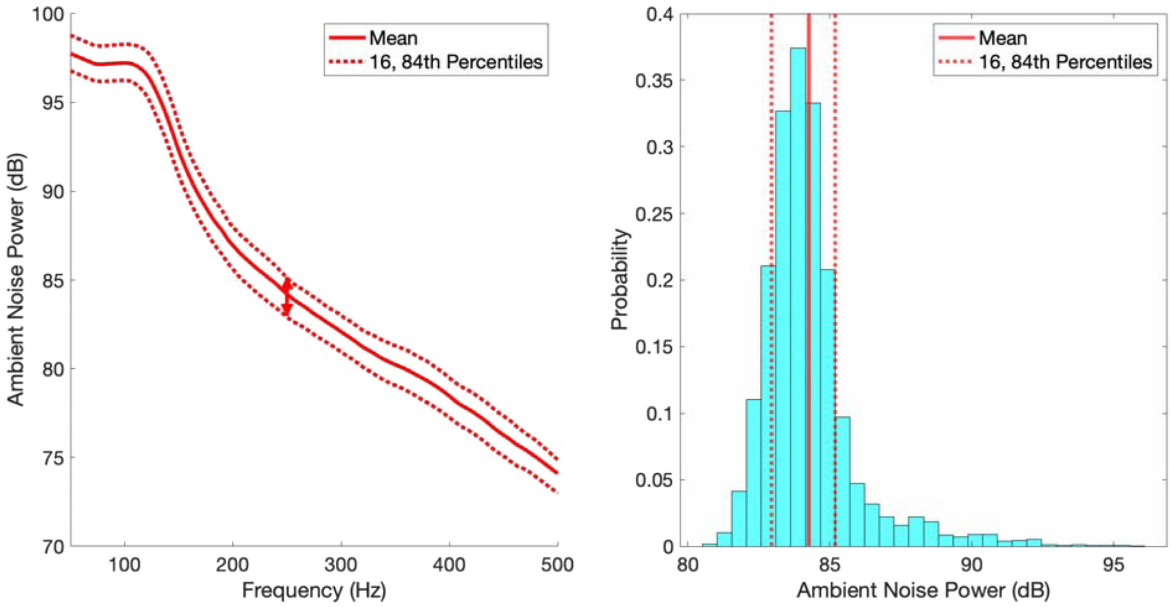

Fig. 10. North survey area measured AN. Left: AN power spectrum from 50 to 500 Hz. Right: AN power distribution in 250 Hz band.

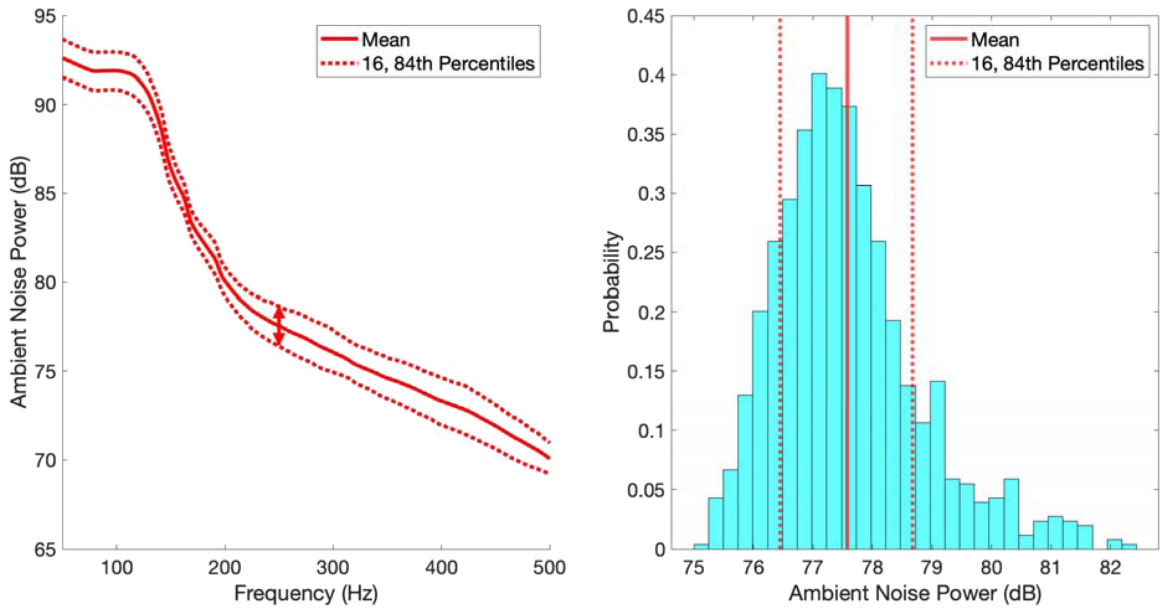

Fig. 11. Southeast survey area measured AN. Left: AN power spectrum from 50 to 500 Hz. Right: AN power distribution in 250 Hz band.

Dyer derives the probability distribution for the natural log of $\langle |p(\omega)|^2 \rangle_{\text{s.t.av.}}$ as

$$P(y) = \left(\frac{1}{2\sigma^2}\right) \exp\left(y - \frac{\exp(y)}{2\sigma^2}\right), -\infty < y \leq \ln\left(\tau^2 N\right). \tag{4}$$

The fluctuations are represented by the standard deviation, which for the above distribution is $\sigma = \pi/\sqrt{6}$. This needs to be converted from σ in natural log $(\ln x)$ to σ_{TL} for TL that is in log base 10. Therefore, we obtain

$$\begin{aligned} \sigma_{TL} &= -10\log_{10}\exp\left(\frac{\pi}{\sqrt{6}}\right) \\ &= -\frac{\pi}{\sqrt{6}}\, 10\log_{10}\exp(1) \approx 5.6\,\text{dB} \end{aligned} \tag{5}$$

as reported in [2]. Interestingly, the mean TL τ as well as the amplitudes A_n and the number of multipath N are significant only for determining the mean value of the pressure field. But, as

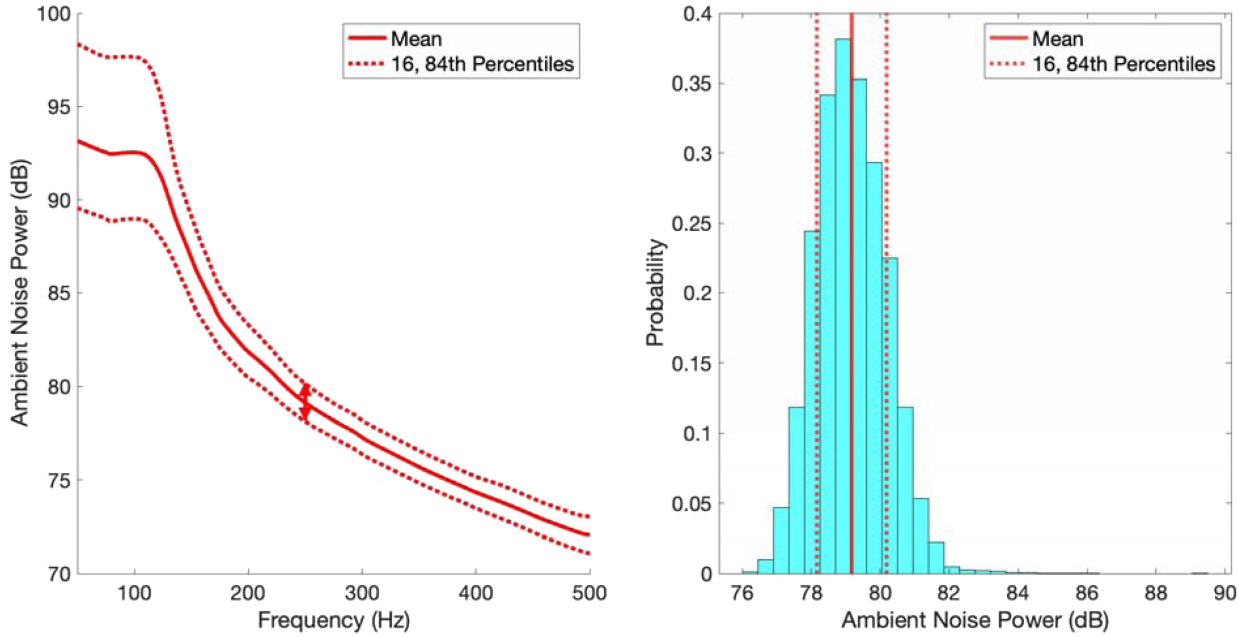

Fig. 12. Southwest survey area measured AN. Left: AN power spectrum from 50 to 500 Hz. Right: AN power distribution in 250 Hz band.

can be seen, the TL fluctuations represented by σ_{TL} is a constant of about 5.6 dB regardless of the other parameters. Here we have also made the simplifying assumption that the Dyer fluctuations are normally distributed.

There are, of course, various ways σ_{TL} can be higher or lower. The time-bandwidth product can play an important role as shown by Makris [22]. The σ_{TL} used here is strictly only valid for time-bandwidth product of one and can be reduced (e.g., to a value close to 2 dB for time-bandwidth product of 10 as shown in [22, Fig. 3]). However, the analysis here can be conducted for any time-bandwidth product by adjusting σ_{TL}. Similarly, σ_{TL} can increase with the inclusion of individual interferers such as nearby ships [2]; however, this baseline value with time-bandwidth of one and no interferers is one that is reasonable to assume in the absence of a different sonar system specification and knowledge about expected interferers.

III. Approach

A. Search Metric Calculation

Assume that a search operation is conducted over a time interval [0,*T*]. Search can be thought of as a sequence of discrete glimpses (as in the case of active sonar pings) or as a continuous looking process (as in passive sonar operations). The *instantaneous probability of detection* Pd(*t*) is the probability that the target is detected at a specific location and time *t* in [0,*T*] under specific sensor-target-environmental conditions. The *cumulative probability of detection*, CPD(*t*) at time *t*, is the probability that the target is detected at least once in the time interval [0,*t*].

Pd(*t*) is computed briefly as follows [23], [24]. For a single passive sensor, mean signal excess $\overline{\text{SE}}$ can be expressed as

$$\overline{\text{SE}} = \text{SL} - \text{TL} - (\text{AN} - \text{DI}) - \text{RD} \tag{6}$$

where SL = source level, TL = transmission loss, AN = ambient noise, DI = directivity index, and RD = recognition differential, all expressed in decibels. RD is defined to be the signal-to-noise ratio at the sensor for which Pd = 0.5. Hence, when $\overline{\text{SE}}(t) = 0$, Pd($t$) = 0.5. Under the assumption that the true signal excess SE equals $\overline{\text{SE}}$ plus a random component

$$\text{SE}(t) = \overline{\text{SE}}(t) + \xi(t). \tag{7}$$

Pd(t) is computed as follows:

$$\text{Pd}(t) = \text{Prob}\{\text{SE}(t) > 0\} = \text{Prob}\{\xi(t) > -\overline{\text{SE}}(t)\}. \tag{8}$$

Following [24], we assume that the fluctuation term, $\xi(t)$, is well represented by a Poisson process. Time intervals between SE "jumps" are given by independent draws from an exponential distribution with mean $1/\lambda$ time units and the fluctuation levels at each jump are drawn from a normal distribution with mean 0 and standard deviation σ. From this, it follows that:

$$\text{Pd}(t) = 1 - \Phi\left(\frac{-\overline{\text{SE}}(t)}{\sigma}\right) = \Phi\left(\frac{\overline{\text{SE}}(t)}{\sigma}\right) \tag{9}$$

where Φ is the cumulative normal distribution function. Note that this σ is equivalent to the Dyer σ_{TL} of Section II-F.

Search effort is generally expended in support of some follow-on action or actions to be executed once a detection occurs. These actions could be military related (e.g., preplanned offensive, defensive, or intelligence collection actions) or nonmilitary related (e.g., actions in support of counting and localizing marine mammal populations). Longer detection ranges are obviously better than shorter ranges; but more significantly, there are often critical ranges at which detection must occur in support of a desired objective. CPD quantifies the likelihood of achieving detections at or outside these critical ranges and hence is of key interest to search planners.

CPD(t) is computed as follows:

$$\text{CPD}(t) = \text{Prob}\{\overline{\text{SE}}(t_0) + \xi(t_0) > 0 \text{ for at least one } t_0 \text{ in } [0,t]\}. \tag{10}$$

In accordance with the Kettelle $\lambda-\sigma$ algorithm [24], the acoustic fluctuation term $\xi(t)$ is modeled here as a $\lambda-\sigma$ process. An associated Monte Carlo approach [24] for computing CPD(t) can be briefly summarized as follows.

1) Compute the mean signal excess $\overline{\text{SE}}(t)$.
2) Assume that the true signal excess $\text{SE}(t) = \overline{\text{SE}}(t) + \xi(t)$.
3) Assume $\xi(t)$ can be modeled as a $\lambda-\sigma$ process, e.g., $\xi(t) \sim N(0, \sigma^2_{\text{SE}})$ with random fluctuation times determined via draws from an exponential distribution with mean $1/\lambda$ time units.
4) Use Monte Carlo methods to model this process and record times when $\text{SE}(t) > 0$ for m-of-n successive looks (in this analysis, we assume a detection occurs when $\text{SE} > 0$ in at least eight of 10 consecutive analysis time steps).
5) $\text{CPD}(t) = N_d/N$, where N_d equals the number of replications satisfying the detection criteria in $(0,t)$ and N equals the total number of replications.
6) In the same fashion, use Monte Carlo methods to compute uncertainty bounds on CPD given estimated model/data uncertainties in mean SE. Uncertainties in mean SE are derived from the results of Sections II-D and II-E.

When modeling a distributed field of receivers, the spatial correlation between receivers must be accounted for. If there was no correlation between receivers, each receiver k would have an independent $\lambda-\sigma$ process $\xi_k(t) \sim N(0,\sigma_k^2)$ as described above. At the other extreme, if the receivers were fully correlated there would be one $\lambda-\sigma$ process $\xi_c(t) \sim N(0,\sigma_c^2)$ common to all receivers. Hence for simplicity, and given the typically large uncertainties associated with real-world acoustic performance prediction parameters, we define ρ to be the correlation between any two receivers in the distributed field and the $\lambda-\sigma$ process at the kth receiver to be

$$\xi(t) = (1-\rho)\,\xi_k(t) + \rho\xi_c(t) \tag{11}$$

where we also assume that

$$\sigma_k = \sigma_c = \frac{\sigma_{\text{SE}}}{\sqrt{1-2\rho+2\rho^2}} \tag{12}$$

so that the overall $\lambda-\sigma$ process $\xi(t) \sim N(0, \sigma^2_{\text{SE}})$. The value of ρ used in this analysis is 0.5; in a real-world analysis, ρ would need to be determined via experimental or analytic means.

B. Receiver Placement Optimization

In this section, we describe a two-step receiver placement optimization that is used to pick N_R receiver placements (latitude, longitude, and depth) that collectively provide optimal sensor coverage over a search area and relevant source depths. The purpose of this optimization is to provide the means for estimating the potential value-added of increased environmental awareness on passive receiver planning and execution effectiveness. The method is necessarily discrete in location and depth since ocean forecast data is also discrete, e.g., the NESBA NCOM forecasts have 1 km × 1 km spatial resolution with 50 depth layers and 3-h forecast time increments. Hence, the resulting receiver placements are optimal relative to the discrete receiver placement grid and assumed discrete source depths (e.g., 25–150 m in steps of 25 m) and associated probabilities that the source would operate at each depth. The optimization employs a Greedy algorithm in Step 1 followed by an integer genetic algorithm (GA) in Step 2 to determine optimal receiver location and depth placements. The Greedy algorithm solution is used to seed the GA initial population matrix. The GA is then used to probabilistically search for the globally optimal placement of N_R receivers.

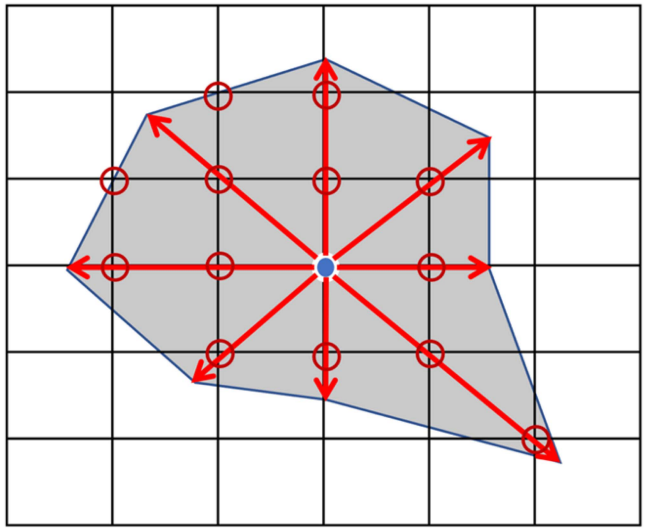

Fig. 13. Area coverage calculation performed for each potential receiver placement p_i and source depth.

It is furthermore assumed that there is an initial source detection, perhaps nonacoustic, at time $T = 0$ with an estimated mean location and associated area of uncertainty (AOU). There is also an assumed associated time $T = t_1$ at which assets could arrive on station for receiver placement operations and an assumed receiver endurance D. Hence, the search operation is assumed to take place in the time interval $[t_1, t_1+D]$. From these assumptions, a search area S is defined encompassing the locus of possible source locations during the search operation time window based on assessed source intentions (e.g., objective destination) and likely source speed of advance. Section IV-A presents a simple example of this search area calculation.

In Step 1, the Greedy placement optimization successively places N_R receivers on the placement grid P formed by the intersection of the NCOM 1 km × 1 km forecast grid and the search area S (in location) and a set of possible receiver depths (e.g., 30, 60, 120, 300 m). The first receiver placement is the node location $p_i \in P$ that provides the maximum area coverage of the search area S summed over all assumed source depths and weighted by the associated source depth probabilities. The area coverage calculation for each source depth is pictured in Fig. 13. The center node location denoted by the blue dot is the latitude and longitude location associated with p_i and the calculation pictured in Fig. 13 is computed for each possible source depth layer. MDR is computed along each of the eight pictured radials (45° – 360° in steps of 45°) based upon the assumed ocean forecast data, AN, and local seabed parameters assumed to be available to the receiver placement decision maker. The coverage "rosette" is the shaded area formed by the polygon connecting

the eight MDR end locations radiating from the location of the p_i node. The area of the rosette can be approximated by the sum of the "area" attribute values of the grid nodes lying within the rosette, which in the case of Fig. 13 is 14 km^2 (since the default "area" attribute of all nodes in a 1 km × 1 km grid = 1 km^2). The optimization metric value associated with placement node p_i is hence given by

$$A_i = \sum_{j=1}^{N_S} a_{ij} \cdot \alpha_j \tag{13}$$

where N_S is the number of source depths considered, a_{ij} is the rosette area for receiver placement p_i and source depth j, and α_j is the probability that the source operates at depth j. The first receiver placement is selected to be the latitude, longitude, and depth node that maximizes this metric over the entire placement grid P.

Once this placement is made, the "area" attribute associated with each node lying within the N_S rosettes (in each of the N_S source depth grids) is reduced from a default value of 1 to 0 km^2. This has the impact of removing any payoff associated with placing subsequent receivers with area coverages overlapping that of the first or other prior receiver placements. Alternate "area" attribute reductions can be used to generate different receiver placement behavior. Subsequent receiver placements are determined in precisely the same fashion as that for the first receiver placement.

In Step 2, the Greedy algorithm solution is then used to seed the GA initial population matrix. The GA, implemented using the MATLAB *ga.m* function, employs the same objective function used in Step 1 Greedy optimization. Note that GA algorithms provide a global optimization technique that often converges to the global minima when applied with the right settings. GAs, however, are completely probabilistic and the goodness of the result depends on the randomness of the process, the length of the chromosomes in individuals, and the number of individuals in the population.

C. Source Motion Optimization

Assume a threat with a level of environmental awareness characterized by an ocean state estimate (e.g., a monthly climatology or an ocean model forecast) and an estimate of omnidirectional AN versus frequency. Also, assume that the threat's initial position is characterized with a spatial uncertainty ellipse and that its objective is to transit to a specific location while minimizing its own likelihood of being counter-detected. In this section, we define an approach for generating threat sample paths consistent with the threat's initial uncertainty ellipse that minimize the threat's chance of being counter-detected (in accordance with its level of environmental awareness) while also achieving its end-state goal of transiting to the objective location.

This problem is solved using Dijkstra's algorithm [25]. Dijkstra's algorithm is an algorithm for finding the shortest (relative to a cost or distance metric) path between nodes in a graph.

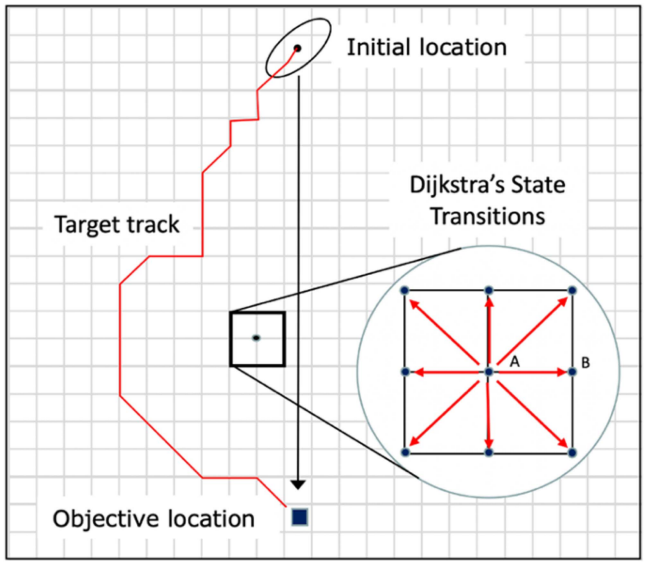

Fig. 14. Source routing graph construction.

We introduce the following standard graph theory definitions [26] to facilitate the discussion of the source motion optimization method employed in this analysis. A graph G is defined as a set of nodes $\bar{N} = (n_1, \ldots, n_p)$, edges $\bar{E} = [(s_1, t_1), \ldots, (s_q, t_q)]$, and edge weights $\bar{W} = (w_1, \ldots, w_q)$, where each s_i and t_j are elements of $\bar{N}$ and the kth element of $\bar{W}$ is the cost associated with edge $E_k = (s_k, t_k)$. A *simple graph* is a graph with at most one edge from any node n_i to any other node n_j.

We construct the threat motion simple graph G as follows.

1) The nodes of G coincide with the 3-D spatial grid spanning the threat's geographic area of interest with 1 km × 1 km × 25 m spacing (latitude × longitude × depth).
2) The edges of G are constructed so that each node A has edges connecting to its eight closest latitude–longitude neighbors as pictured in Fig. 14.
3) The weight of each node A to node B edge is equal to the threat counter-detection potential at node B across all possible receiver depths. This potential is captured by computing the fraction F of nodes within 5 km of B, for each receiver depth, that are within MDR of B. Higher values of F are indicative of higher likelihoods of source counter-detection.
4) In addition, each A to B edge has an assumed target depth equal to the best (i.e., minimum counter-detection potential) source depth (evaluated at B) with respect to the source's assumed environmental awareness.

Once graph G has been constructed, Dijkstra's algorithm [25] can be employed to find the shortest path (where shortest = minimum summed counter-detection potential) from any starting node m to any destination node n [27]

$$\left[\bar{E}_{m|n}, c_{m|n}\right] = \text{shortestpath}\,(G, m, n) \tag{14}$$

where $\bar{E}_{m|n}$ is the vector of edge indices associated with the shortest path and $c_{m|n}$ is the total cost associated with $\bar{E}_{m|n}$.

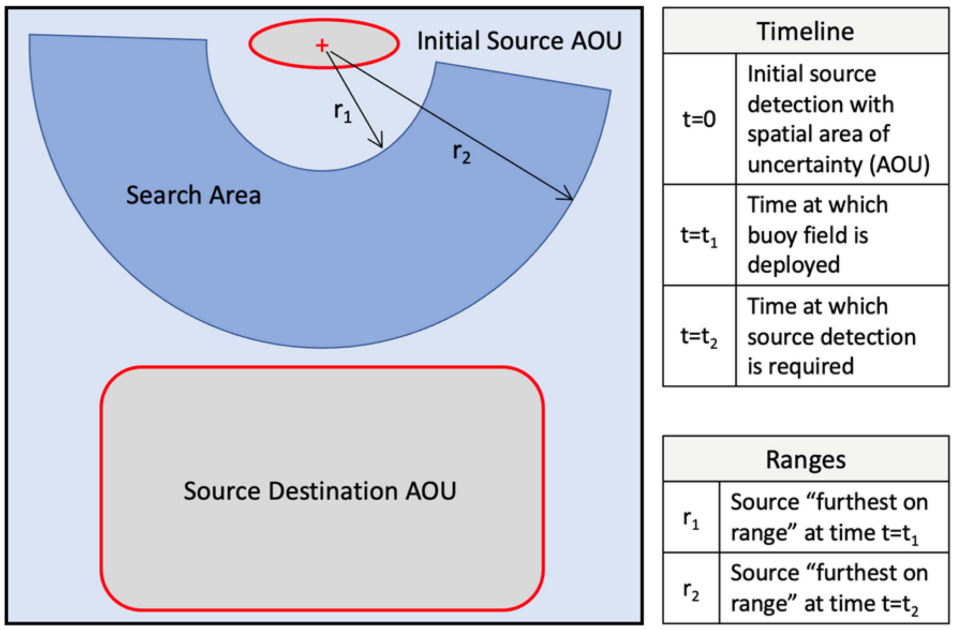

Fig. 15. Sample problem geometry.

A modified version of Dijkstra's algorithm can find the shortest path from all nodes in G to any destination node n in G [27]

$$\left\{\left[\bar{E}_{m|n}, c_{m|n}\right],\ m = 1 \ldots p\right\} = \text{shortestpathtree}\,(G, n) \tag{15}$$

where again $\bar{E}_{m|n}$ is the vector of edge indices associated with the shortest path from node m to node n and $c_{m|n}$ is the total cost associated with $\bar{E}_{m|n}$.

IV. Results

A. Sample Problem

The goal of this article is to demonstrate the potential utility of the optimal configuration of a field of passive receivers versus an environmentally aware source with end-state goals, leveraging the data collected during the Spring of 2021 NESBA Signals and Noise Experiment. This optimization is designed to provide an acoustic system operator with actionable guidance relating to optimal distributed receiver locations and depths and likely mean source detection times and associated uncertainties as a function of source and receiver levels of environmental awareness. This demonstration is conducted in the context of the sample problem illustrated in Fig. 15. In this problem, it is assumed that the source is detected, perhaps nonacoustically, at time $t = 0$ with the area AOU pictured in the figure. It is assumed that follow-on acoustic search assets are available such that it is feasible to deploy a distributed field of passive receivers by time $t = t_1$ and that the search goal is to redetect the source as quickly as possible but no later than time $t = t_2$. The environmental awareness of the sonar operator in the baseline or "pre-NESBA" case is assumed to be based on a single CTD measurement and *database* values for AN and seabed parameters. In the enhanced or "NESBA" case, sonar operator awareness is assumed to be based on the NESBA NCOM baseline forecast (described above in Section II-B) and NESBA *measured* AN (see Section II-E) and *measured* seabed parameters (see Section II-C).

The source is assumed to have the goal of transiting to a specific location within the pictured source destination AOU as quickly as possible while minimizing the chances of being counter-detected. Two source environmental awareness cases are considered: in the first, source environmental awareness is based on climatology [e.g., Generalized Digital Environmental Model (GDEM) [28]] and in the second, source awareness is based on forecast data from a global ocean model (e.g., Global Hybrid Coordinate Ocean Model (HYCOM) [29] or equivalent). In both cases, source AN and seabed parameters are derived from standard databases.

The search area is defined to be the area between an arc centered on the initial source AOU with radius r_1 equal to the likely source "furthest on range" at time $t = t_1$ and the arc (also centered on the initial source AOU) with radius r_2 equal to the likely source "furthest on range" at time $t = t_2$, as pictured in Fig. 15.

The ground truth ocean environment is assumed to be well represented by the NCOM nature environment described in Section II-B.

In this illustration, it is assumed that 30 receivers can be deployed within the search area, each at one of four possible depths (30, 60, 120, 300 m), and that the source can operate at any one of six possible depths (25, 50, 75, 100, 125, 150 m). We also assume that receiver monitoring capabilities exist sufficient to receive data from all receivers simultaneously during the search operation.

Table III summarizes the sonar operator and source cases considered in the remainder of this section.

TABLE III
SOURCE AND RECEIVER CASES CONSIDERED

Case	Sonar Operator Assumptions	Source Assumptions
Baseline (pre-NESBA)	– Environmental awareness based on a single CTD measurement – Database AN (e.g., Wentz [9]) – Database seabed parameters (e.g., bottom sediment type BST database [30])	Environmental awareness based on GDEM [28] or equivalent
		Environmental awareness based on global HYCOM [29] or equivalent
Enhanced (NESBA)	– Environmental awareness based on NESBA NCOM baseline forecast (see Section II-B) – AN derived from NESBA measurements (see Section II-E) – Seabed parameters derived from NESBA measurements (see Section II-C)	Environmental awareness based on GDEM [28] or equivalent
		Environmental awareness based on global HYCOM [29] or equivalent

TABLE IV
SOURCE MOTION CASES AND ACOUSTIC MODELING ASSUMPTIONS

Case	Oceanography	Seabed	AN	Counter-Detection Awareness
A	GDEM	BST database [30] or equivalent	Wentz curve data [8] or equivalent	Source assumes that opposition force will use passive buoys with known acoustic parameters to re-detect
B	HYCOM			
C	NCOM Baseline			
D	NCOM Nature			

B. *Source Motion Versus Environmental Awareness*

In this section, we present the results of the source motion optimization algorithm described in Section III-C as applied to NESBA forecast data generated on May 5, 2021 for GMT hours 000 to 003. Early May 2021 was a NESBA time-period during which frequent CTD measurements were taken. Source motion is computed here for the two levels of source environmental awareness listed in Table III.

1) *GDEM:* GDEM [28] is a 4-D (latitude, longitude, depth, month) database of average temperature and salinity versus depth profiles. Most relevant sources could be expected to have knowledge of GDEM or equivalent.
2) *Global HYCOM:* HYCOM [29] is the Navy's operational global ocean forecast model. Some relevant sources may have occasional access to forecast data from a global ocean model such as HYCOM or equivalent.

In addition, for comparison purposes, source motion results are also presented here assuming that the source has environmental awareness equivalent to that provided by the NESBA NCOM baseline and nature forecasts. Relevant acoustic modeling assumptions for each of these source motion cases are provided in Table IV. Source knowledge of the seabed is assumed to be equivalent to data contained in the BST database and source knowledge of AN equivalent to Wentz curves. The source is also assumed to correctly guess that the opposition will try to counter-detect with passive buoys and acoustic processing having known capabilities.

The detailed computational steps required to execute optimal source motions are as follows.

1) Employ the RAM [20], [21] to compute gridded TL data over the entire operations area pictured in Fig. 15 as a function of source latitude and longitude, source-to-receiver radial (0°–360° in steps of 45°), receiver depth, source depth, and source-to-receiver range.
2) Compute gridded MDR (i.e., $\overline{\mathrm{SE}} = 0$ range) as a function of source latitude, longitude, and depth, receiver depth, and source-to-receiver radial. MDR also depends upon AN, RD, and DI.
3) Compute gridded best source depths and associated minimum MDR values (averaged over all receiver depths and radials) as a function of source latitude and longitude. Best source depth is the source depth with minimum counter-detection MDR, indicative of a high loss and/or high AN path, and hence minimum counter-detection potential.

These minimum MDR values are used to compute the Dijkstra graph edge weights as discussed in Section III-C and associated best source depths are used to set the source depths associated with each graph edge.

Fig. 16 shows the minimum MDR values (again averaged over all receiver depths and radials) interpolated to 1 km spatial resolution (left panel) and best source depths (right panel) for

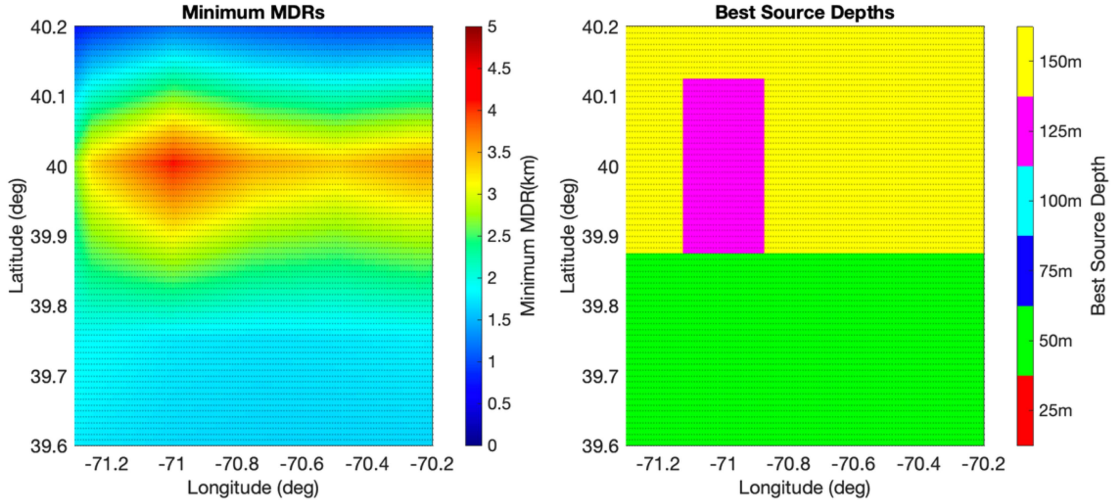

Fig. 16. GDEM minimum mean MDRs (left) and best source depth (right).

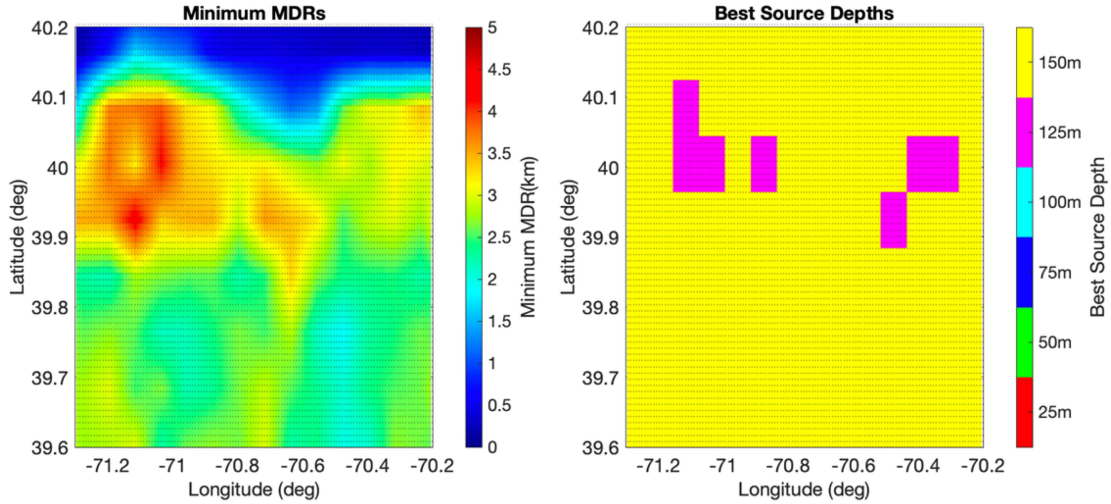

Fig. 17. HYCOM minimum mean MDRs (left) and best source depth (right).

GDEM. Fig. 17 shows the same information for HYCOM. For the sake of comparison, Figs. 18 and 19 show the same information for NCOM baseline and NCOM nature, respectively. The effects of GDEM low spatial resolution (∼30 km) versus HYCOM medium spatial resolution (∼10 km) versus NCOM high spatial resolution (∼1 km) are readily apparent in these four figures. There is general consistency, however, from GDEM to HYCOM to NCOM baseline and nature forecasts. Note again that these minimum MDR and corresponding best source depth values are used to determine Dijkstra edge weights and associated source depths.

For GDEM- or HYCOM-based source motion (the two cases considered in the analysis that follows), source motion in the search area pictured in Fig. 15 (with latitudes greater than 39.9N) has best source depths greater than or equal to 125 m (i.e., 125 m or 150 m). These depths correspond to GDEM or HYCOM predicted minimum MDRs and hence minimum potential for counter-detection. It will be assumed in the distributed receiver placement optimization calculations described in Section IV-C that the opposing sonar operator recognizes that the source is most likely to operate at these depths.

Figs. 20–23 show in the left panel the source initial AOU (red ellipse) and destinations (random locations denoted "+" in the southern half of the search area) and in the right panel the resulting optimal source routes from the center of the source initial AOU (white lines) for GDEM, HYCOM, NCOM baseline, and NCOM nature, respectively. CPD is computed as a Monte Carlo simulation for random source starting locations within the initial AOU and random destination locations within the source destination AOU.

C. *Distributed Receiver Placements*

In this section, we present the results of the receiver placement optimization algorithm described in Section III-B, as applied to NESBA forecast data generated on May 5, 2021 for GMT hours 000 to 003. Receiver placements are computed here for the two levels of receiver operator environmental awareness described

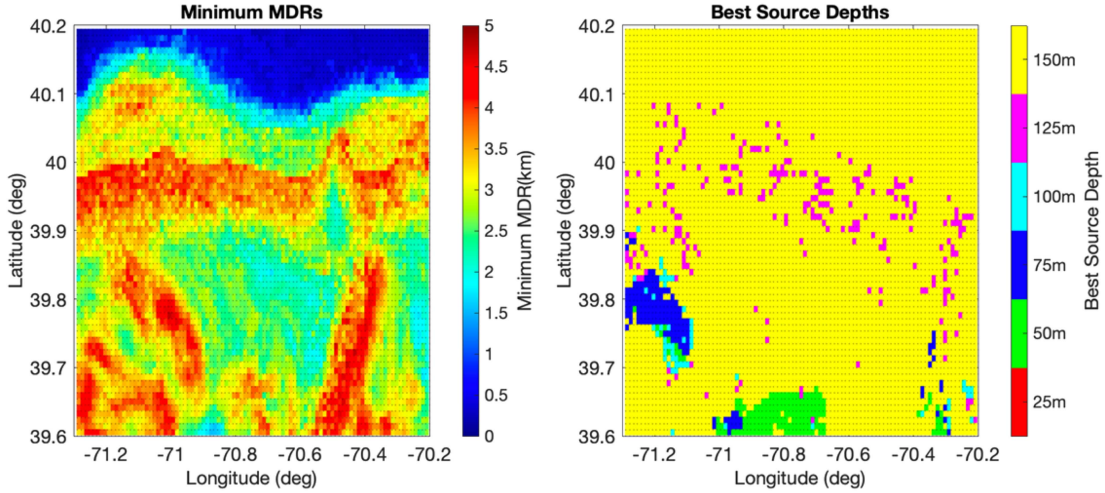

Fig. 18. NCOM baseline minimum mean MDRs (left) and best source depth (right).

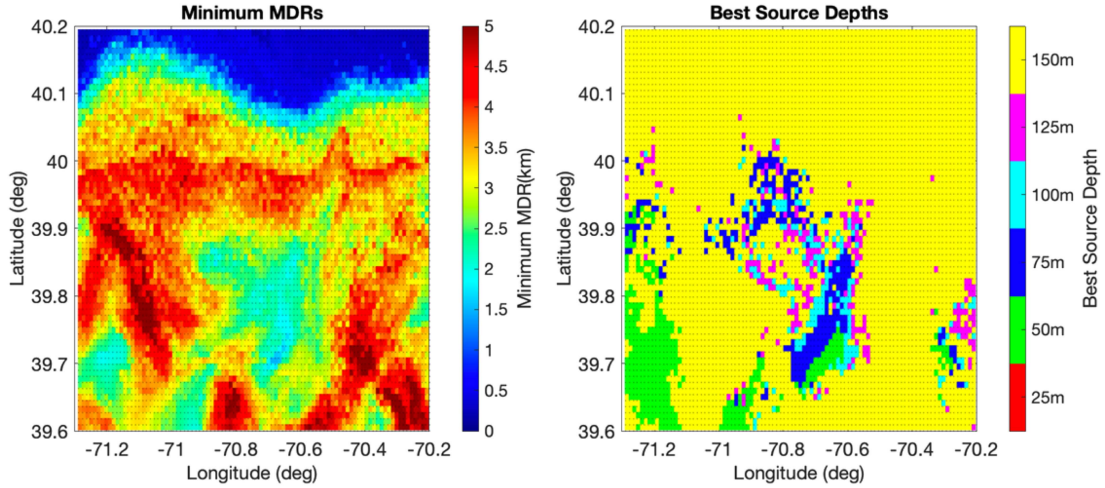

Fig. 19. NCOM nature minimum mean MDRs (left) and best source depth (right).

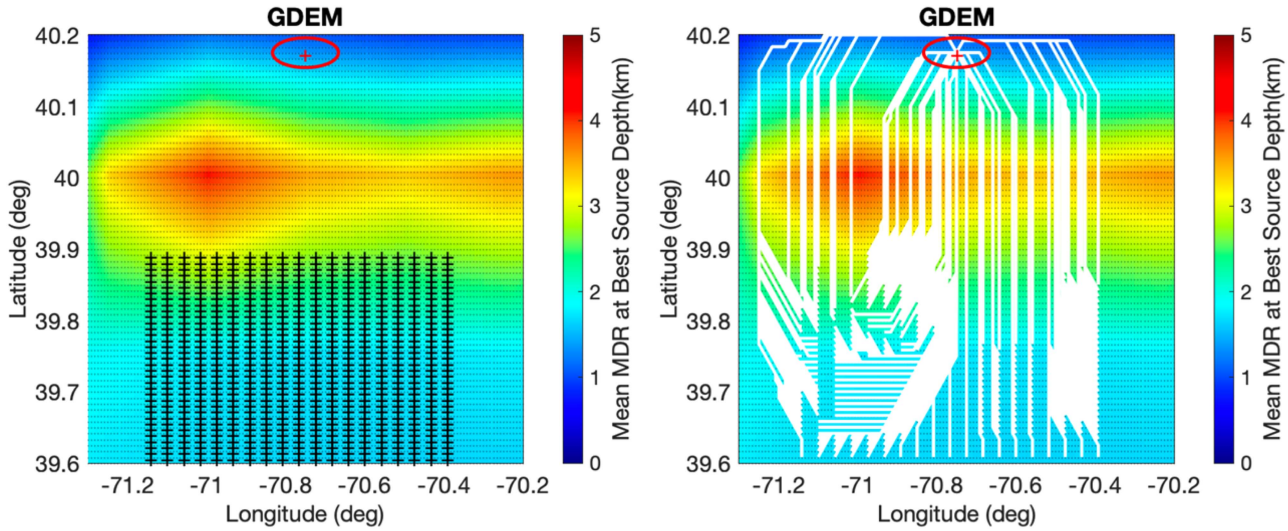

Fig. 20. Source initial AOU and destinations (left) and illustrative GDEM based optimal routes (right).

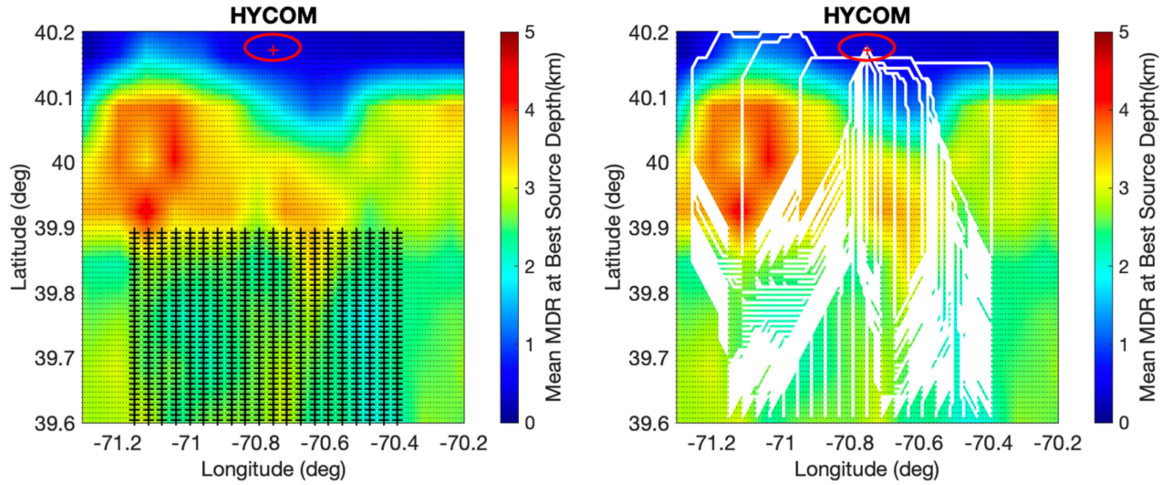

Fig. 21. Source initial AOU and destinations (left) and illustrative HYCOM based optimal routes (right).

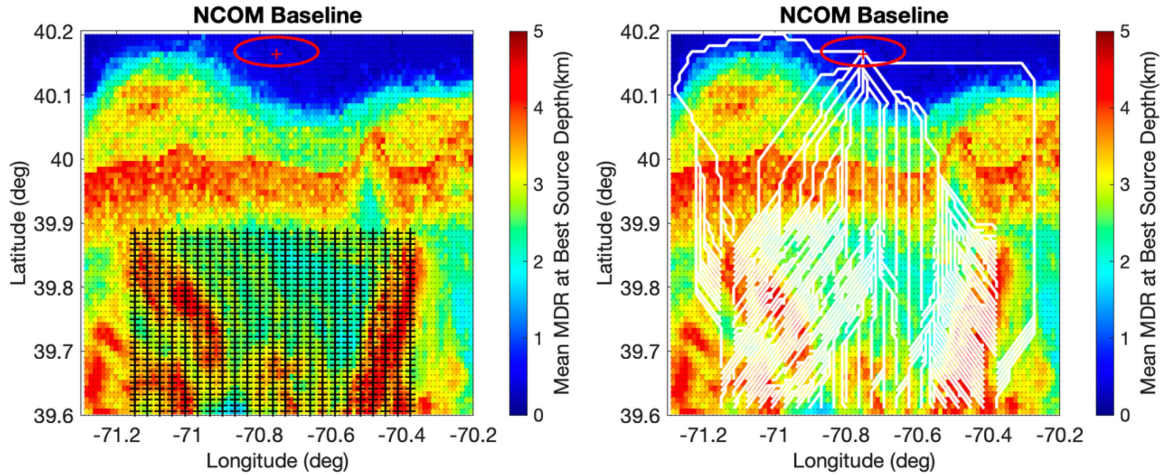

Fig. 22. Source initial AOU and destinations (left) and illustrative NCOM Baseline based optimal routes (right).

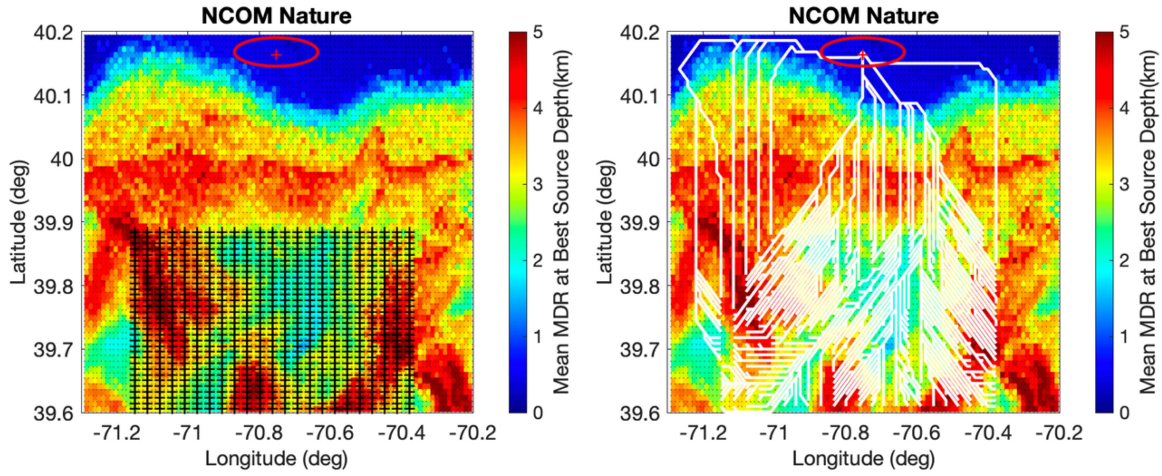

Fig. 23. Source initial AOU and destinations (left) and illustrative NCOM Nature optimal routes (right).

TABLE V
RECEIVER PLACEMENT CASES CONSIDERED

Case	T/S	Seabed	AN	Source Behavior Awareness
Pre-NESBA: Uniform Spacing and Depth	One simulated CTD measurement drawn from NCOM nature environment	BST database or equivalent	Wentz curve data or equivalent	Source highly likely to operate deep (>= 125 m)
NESBA: Non uniform Spacing and Depth	NCOM Baseline ensemble forecast	NESBA measured seabed parameters	NESBA measured AN level	Source highly likely to operate deep (>= 125 m)

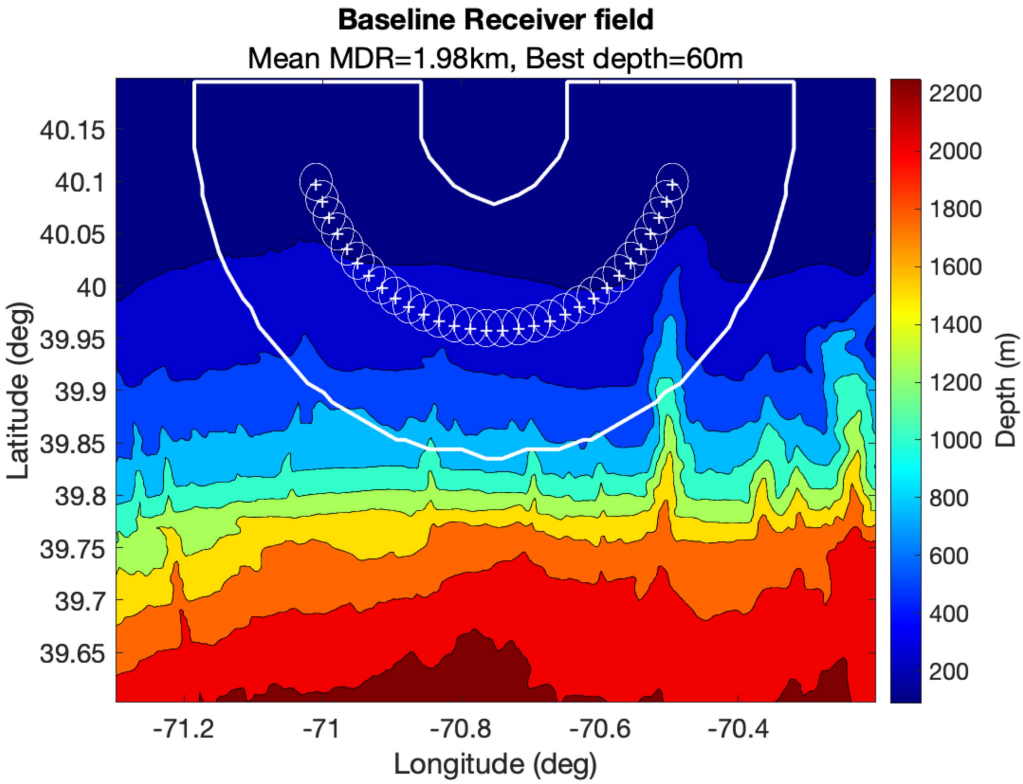

Fig. 24. Baseline (pre-NESBA) receiver placements with bathymetry overlay.

in Table III. Two receiver placement methods are evaluated as described below and summarized in Table V.

1) *Baseline (pre-NESBA):* In the baseline case, when only one (or a few) CTD measurements are assumed to be available, a simulated CTD is used to compute a typical MDR and best depth that are used to characterize the full search area. In this case, one might reasonably decide to deploy the receiver array with uniform spacing (where spacing = some multiple of MDR) and uniform depth. The simulated CTD measurement is sampled from the NCOM nature forecast (since this is assumed here to represent the true ocean state) within the search area pictured in Fig. 15. The CTD measurement location is selected to coincide with average receiver detection capabilities within the search area versus a source operating at its best depth. An MDR for each receiver depth at the CTD measurement location is computed as an average over all radials and relevant source depths and the receiver depth with the greatest average MDR is selected as the depth of the receiver array.
2) *Enhanced (NESBA):* In the enhanced case, we assume that the NCOM baseline forecast is known, which is employed with the receiver placement optimization described in Section III-B to determine optimal receiver locations and depths within the search area pictured in Fig. 15. In this calculation, the source is assumed to be operating at its best depth, which in this case is 125 or 150 m, as discussed in Section IV-B.

Fig. 24 shows the baseline (pre-NESBA) single CTD measurement-based receiver placements and (single) depth. In

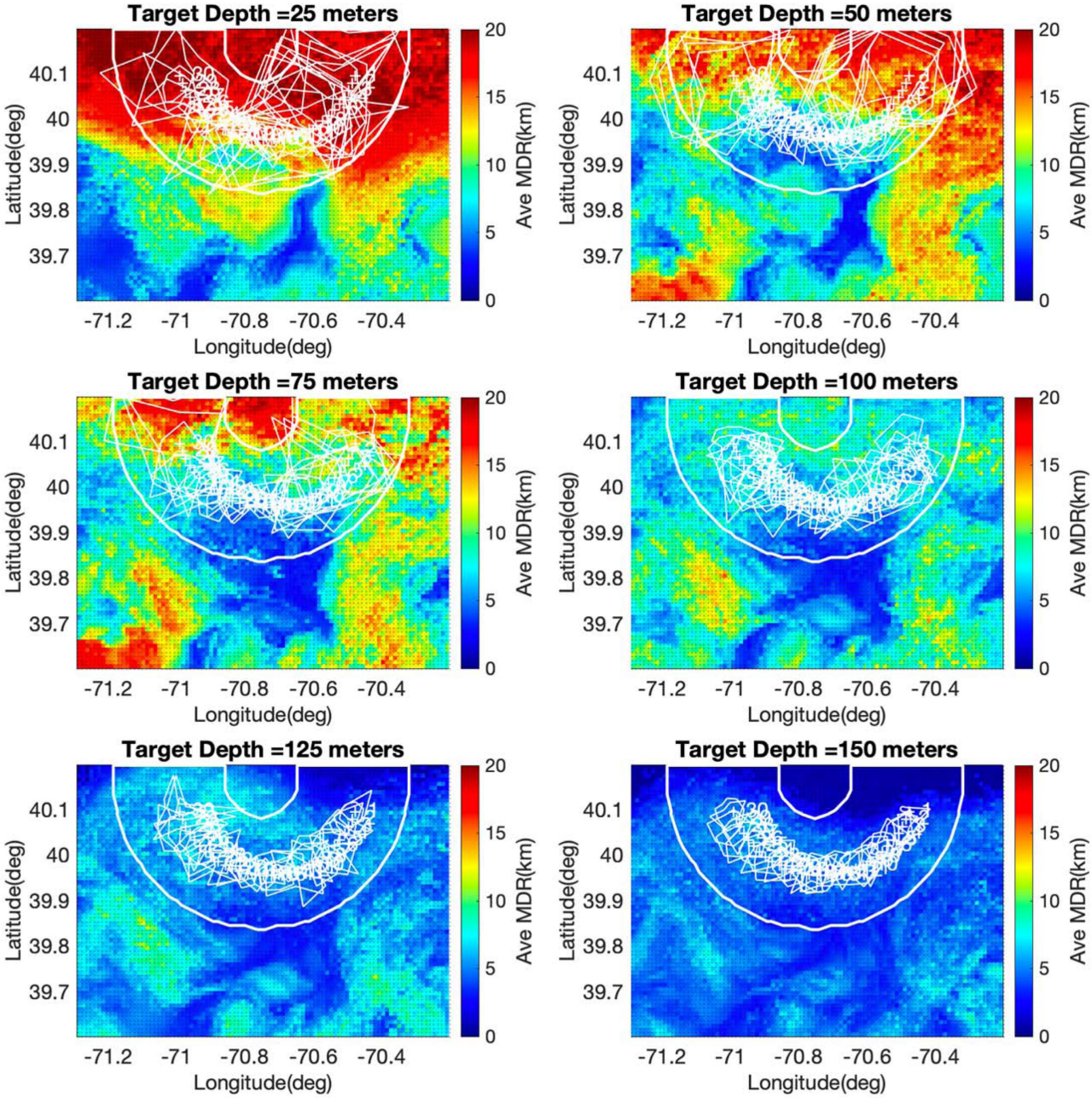

Fig. 25. Baseline (pre-NESBA) receiver MDR rosettes for each source depth.

this case, the MDR associated with the simulated CTD measurement is 1.98 km and the associated best receiver depth is 60 m. An arced east-west oriented barrier is deployed midway between the inner arc (positioned 5 nm from the initial source AOU center) and the outer arc (positioned 20 nm from the AOU center). Receiver spacing is assumed to be equal to 1 × MDR.

Fig. 25 shows the individual receiver MDR rosettes associated with each baseline receiver location versus each source depth. The rosette at each receiver location is formed by the latitude–longitude polygon with corners formed by the one MDR end points along the eight radials emanating from the receiver location at 45°–360° in steps of 45°. Note again that under the source environmental awareness assumptions (GDEM or HYCOM) described in Table IV, best target depths in the search area are limited to 125 or 150 m.

Fig. 26 shows the enhanced NESBA optimal receiver placements and depths with receiver depths noted in meters. Sonar operator environmental awareness is assumed to be based on the NCOM baseline forecast. Fig. 27 shows the individual receiver MDR rosettes associated with each optimal (NESBA) receiver location and depth versus each target depth. Note again that under the target environmental awareness assumptions (GDEM or HYCOM) described in Table IV, best target depths in the search area are limited to 125 or 150 m. The color overlays show best MDR values (averaged over all radials) versus location and source depth.

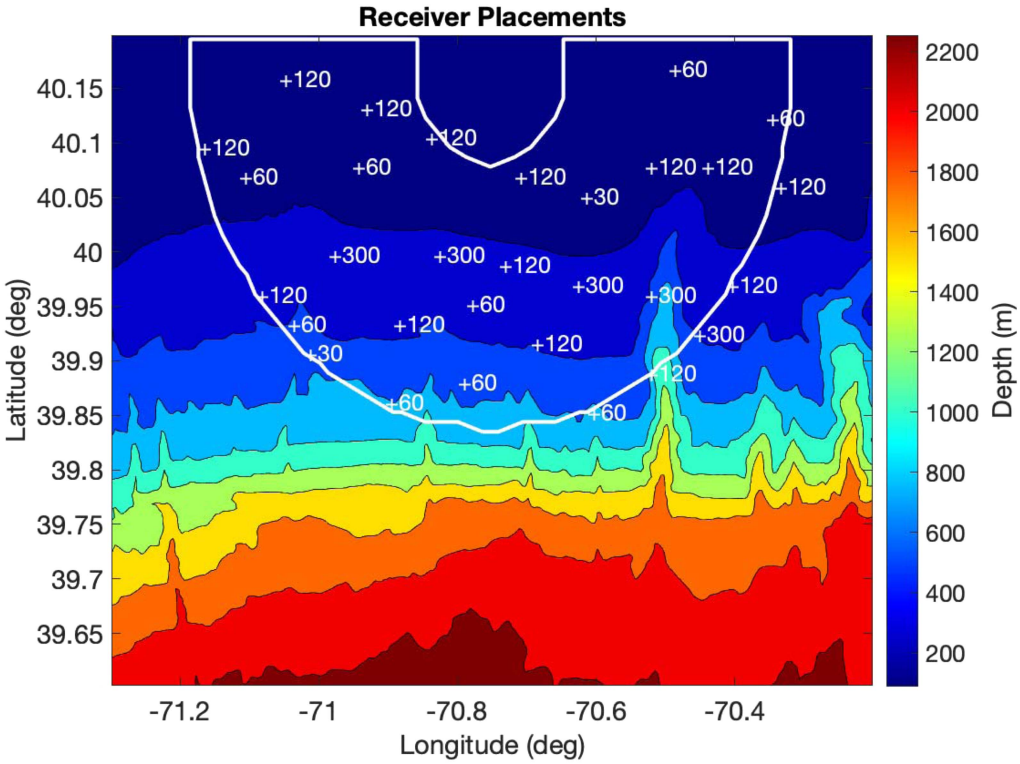

Fig. 26. Optimal (NESBA) receiver placements with bathymetry overlay and receiver depths noted in meters.

Inspection of Figs. 25 and 27, for relevant source depths 125 and 150 m, provides a visual capture of the impact of the receiver optimization algorithm. For target depths 125 and 150 m, the optimal (NESBA) receiver placements in Fig. 26 provide significantly more search area coverage versus the baseline (pre-NESBA) receiver placements shown in Fig. 24. The search effectiveness impact of this is quantified for this example in the following section in terms of the CPD metric.

D. Operational Effectiveness Metrics

In this section, we present the CPD results for the four source and receiver cases described in Table IV. CPD is computed in accordance with the search metric calculation approach described in Section III-A. These results are based upon the following input data assumptions.

1) *Ground Truth Ocean State:* SE calculations are based upon the NCOM nature forecast (see Section II-B), which is used here as the best representation of true ocean state.
2) *Mean SE:* Mean SE is computed based on range-dependent TL and NESBA measured AN (see Section II-E).
3) *SE Fluctuation Statistics:* SE fluctuation statistics are modeled as described in Section II-F.
4) *Uncertainty in Mean SE:* Uncertainty in mean SE is computed based on NESBA seabed measurements (see Section II-C), NCOM ensemble forecasts (see Section II-B), and NESBA AN measurements (see Section II-E).
5) *Monte Carlo Replications:* These CPD results are based on 5000 Monte Carlo replications. Each replication assumes a randomly selected source track (see Figs. 20–23) and the optimal receiver placements and depths (Fig. 26) in the enhanced (NESBA) case or the baseline placements and depths (Fig. 24) in the baseline (pre-NESBA) case.

Fig. 28 shows CPD results for optimal receiver placements and depths (left panel) versus baseline (single CTD) receiver placements and depths (right panel) in the Southwest survey area assuming source routing is based upon GDEM. These plots show CPD versus range in km from the center of the initial source AOU. The solid blue line shows mean CPD versus range and the blue shaded area shows CPD uncertainty bounds (16 and 84 percentiles). In the optimal placement case, a high confidence CPD of 0.5 is attained at 12 km from the AOU center, whereas in the baseline case, a highly uncertain CPD of 0.5 is not attained until approximately 21 km from the AOU center. Optimal receiver placements and depths hence provide substantial operational value-added when the source routing is based on GDEM. The uncertainty reduction in the optimal placement case is due to the use of NESBA seabed and AN measurements and NCOM ensemble forecasts. The larger uncertainties in the baseline placement case are due to the use of seabed, oceanography, and AN database derived estimates versus measurements.

Similarly, Fig. 29 shows CPD results for optimal receiver placements and depths (left panel) versus baseline (single CTD)

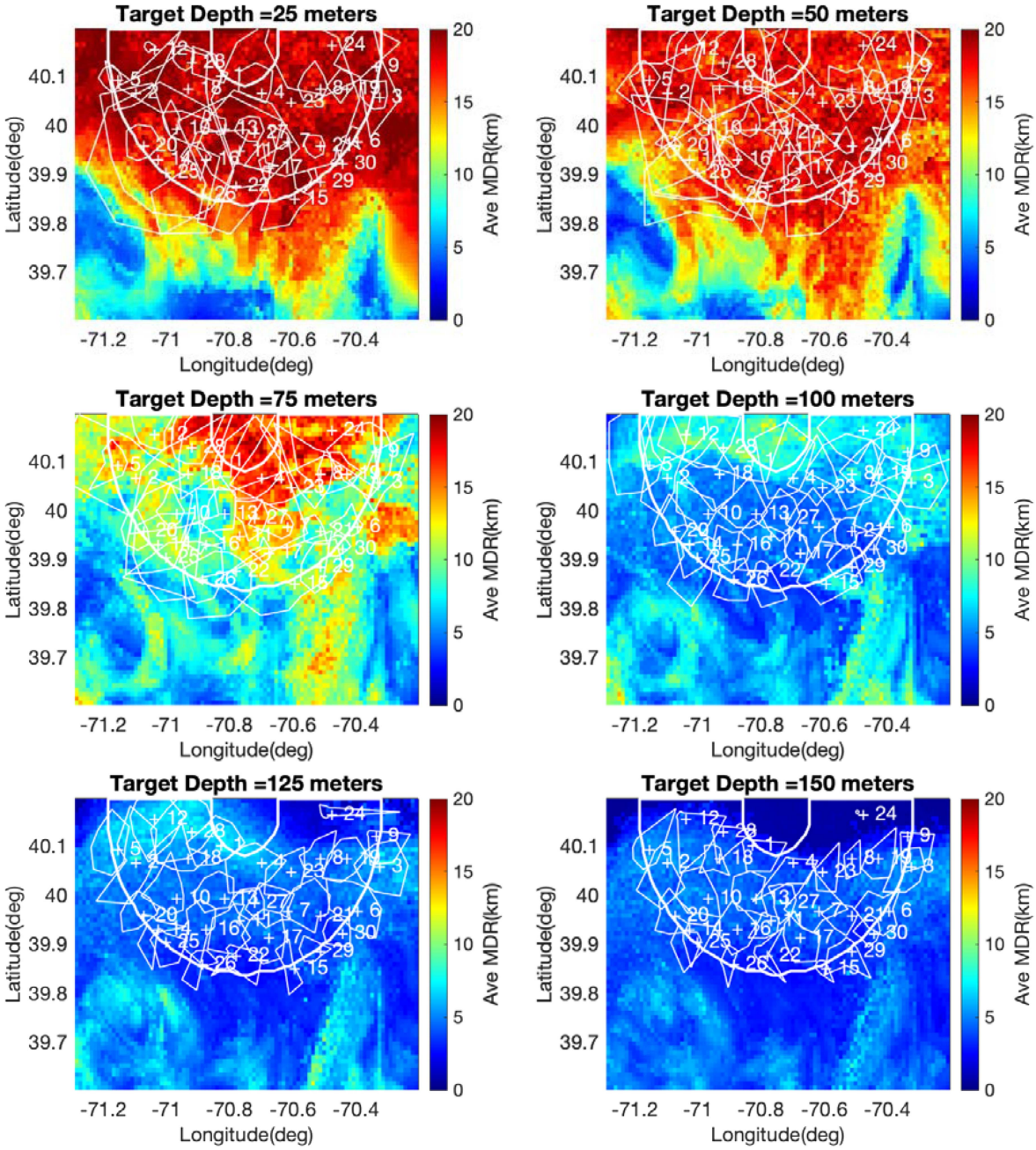

Fig. 27. Optimal (NESBA) receiver MDR rosettes for each source depth.

receiver placements and depths (right panel) in the Southwest survey area assuming source routing is based upon global HYCOM. In this case, there is still CPD range and uncertainty reduction in the optimal placement case, but it is lessened due to the assumption that the source has access to global HYCOM (or equivalent) forecasts for routing.

Finally, Fig. 30 shows CPD results for optimal receiver placements and depths (left panel) versus baseline (single CTD) receiver placements and depths (right panel) in the Southwest survey area assuming source routing is based upon the NCOM baseline forecast. In this case, there is still uncertainty reduction in the optimal placement case, but CPD range improvements are largely eliminated due to improved source environmental awareness.

V. Discussion

In this article, we have demonstrated an approach for the optimization of a field of passive receivers versus an environmentally aware source with end-state goals. This optimization is designed to provide an acoustic system operator with actionable guidance relating to optimal distributed receiver locations and depths and likely mean source detection times and associated uncertainties as a function of source and receiver levels of environmental

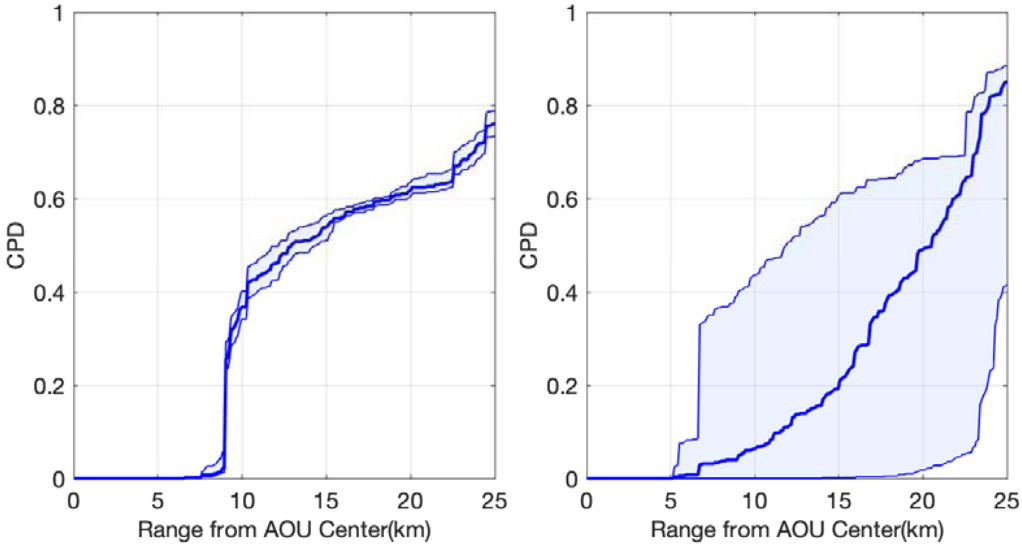

Fig. 28. CPD results for optimal (left panel) versus baseline (right panel) receiver placements and source routing based on GDEM.

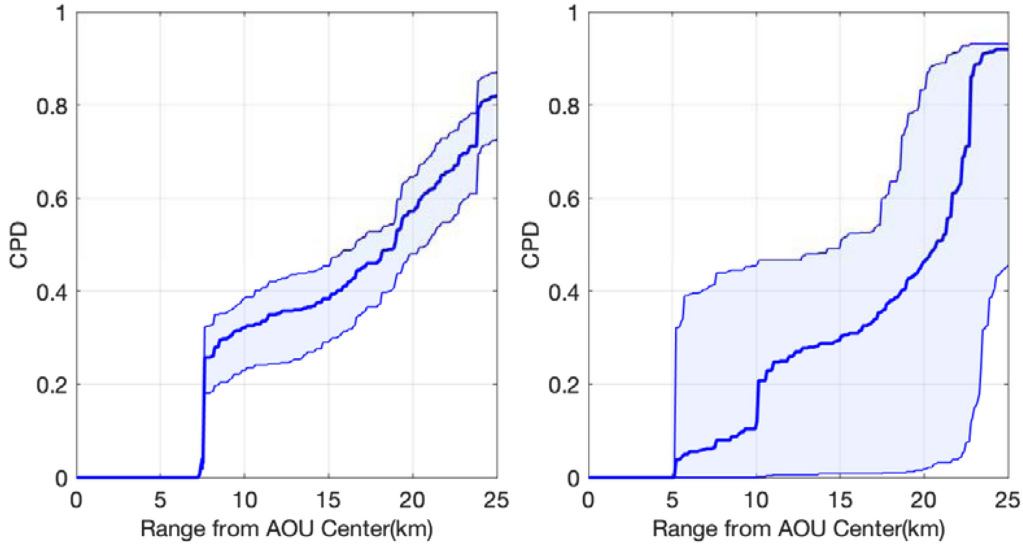

Fig. 29. CPD results for optimal (left panel) versus baseline (right panel) receiver placements and source routing based on HYCOM.

awareness. The main contribution of this work pertains to the use of advanced ocean modeling and environmental sensing in the capture of operational metric uncertainties while accounting for source and receiver levels of environmental awareness versus the specific optimization approach employed. Specifically, NESBA experimental data has been used to estimate TL uncertainties due to uncertainties in oceanography (using NCOM ensemble forecast data) and seabed characteristics (using passive seabed characterization measurements) and AN levels and uncertainties due to winds, waves, and the presence of fishing/shipping traffic. The statistics of random statistical fluctuations in received signal due to moving inhomogeneities in the sea (caused by source and receiver motion as well as surface and internal waves) have been estimated based on the work of Dyer [2].

It is also important to note that while this demonstration has been conducted for relatively simple source and receiver behaviors and geometries (that of a point A to point B source with environmental awareness versus distributed passive receivers) and analysis objective (select best passive receiver locations and depths), this methodology is not limited to this case and could be extended to more general operational situations as follows.

1) *Source Behavior:* Different source behaviors can be considered including optimal or probabilistic depths and approach tracks or sectors. Multiple source frequencies and source levels can be accounted for.
2) *Receiver Types:* The methodology demonstrated here for combining advanced ocean modeling and environmental sensing with a passive receiver optimization can be

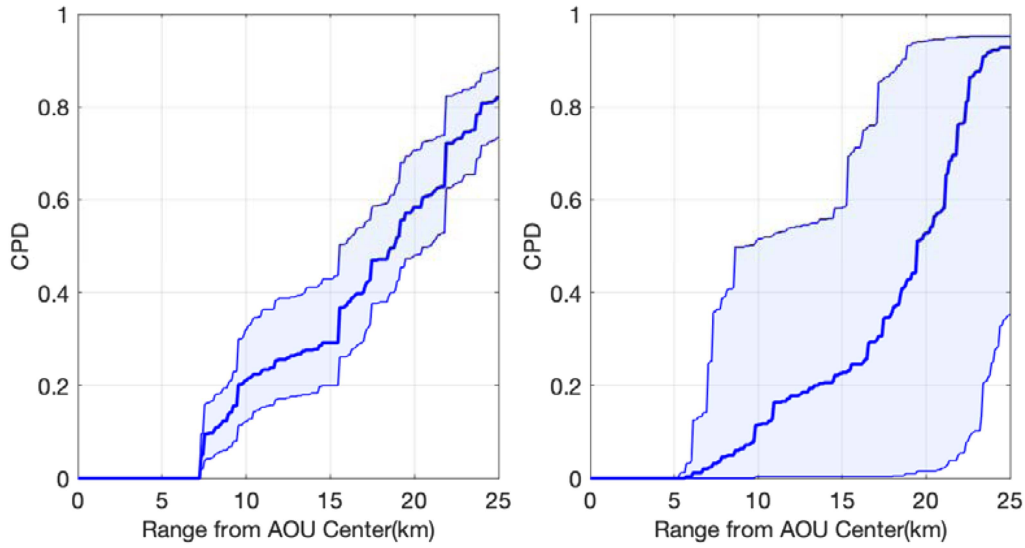

Fig. 30. CPD results for optimal (left panel) versus baseline (right panel) receiver placements and source routing based on NCOM baseline.

extended for use with more complex optimization approaches for other types of distributed receivers, e.g., bistatic or multistatic acoustics.

3) *Operational Situations:* The methodology can be applied to a wide range of operational situations including but not limited to area search, barrier search, screening, and intelligence collection operations.
4) *Analysis Objectives:* Possible applications of this methodology include but are not limited to receiver configuration optimization, source behavior optimization, and assessment of the likely impact of enhanced environmental awareness due to projected enhancements in ocean environment modeling and sensing.

Finally, it is also important to note that the acoustic measurements and modeling employed here, including high-resolution NCOM ensemble forecasts, are current operational capabilities available to industry, government, and military end users. In addition, the CPD calculation approach proposed here is ideally suited to ashore cloud-based computing with landline connectivity to sources of ensemble forecast data. Low-bandwidth end-user prediction requests and result dissemination are well suited to shipboard user support.

VI. Conclusion

The conclusions we have drawn from this work can hence be briefly summarized as follows.

1) Deterministic sonar performance predictions can be highly misleading due to typically high levels of uncertainty in TL and AN as well as other factors impacting the calculation of SE. Despite this fact, ocean acoustic predictions are not generally presented to acoustic system operators with uncertainty bounds.
2) CPD is a widely accepted operational metric applicable to a broad range of sonar system use cases. Current generation onboard and offboard environmental measurement and ocean modeling capabilities can be leveraged to compute CPD with explicit estimates of total and marginal (due to uncertainties in oceanography, seabed, and AN) uncertainty.
3) Recent advances in ocean sensing and modeling are applicable to this methodology:
   a) High-resolution ocean modeling with ensembles can be used to span the likely space of possible ocean states thus capturing oceanographic uncertainty levels.
   b) A wide range of onboard and offboard acoustic systems can be employed to measure and monitor directional AN.
   c) Low-cost onboard and offboard through-the-sensor sensing and processing systems are available for rapid in situ seabed characterization and uncertainty estimation.
4) Distributed sensor optimization approaches can be successfully coupled with advanced ocean modeling and enhanced environmental sensing to yield substantial improvements in distributed sensor performance and performance estimation with explicit quantification of relevant performance uncertainties.

Appendix
NCOM and Navy Coupled Ocean Data Assimilation (NCODA) Three-Dimensional Variational (3DVAR) System

NCOM is the operational regional ocean model for the US Navy. NCOM is a primitive equation model and uses the hydrostatic and Boussinesq approximations. NCOM has a free surface with terrain-following sigma surfaces overlaid on constant depth-level surfaces in the interior. The model configuration for the work shown here employed the Mellor–Yamada Level-2.5 turbulence closure [31] with a third-order upwind horizontal advection scheme that is naturally diffusive (no explicit diffusion scheme is used). Lateral boundary conditions are provided by

the Global Ocean Forecasting System v3.1, which uses the HYCOM at 1/12° horizontal resolution and the NCODA for data analysis [32]. Surface atmospheric forcing is provided by the Navy's operational global atmospheric model, the Navy Global Environmental Model [33] at three-hourly intervals. The NCOM domain used here covers a roughly 6° × 6° region just south of the New England coast from 73.0° W to 67.0° W longitude and 37.0° N to 42.5° N latitude (see Fig. 3). The domain has 1 km horizontal resolution with 50 vertical levels (25 sigma levels) extending past 4500 m depth in the deepest part of the domain.

The data assimilation software used in this work is NCODA, which utilizes a 3DVAR method [32]. NCODA-3DVAR solves the following analysis equation:

$$\mathbf{x}_a = \mathbf{x}_b + \mathbf{B}\mathbf{H}^{\mathrm{T}}\left(\mathbf{H}\mathbf{B}\mathbf{H}^{\mathrm{T}} + \mathbf{R}\right)^{-1}\left[\mathbf{y} - \mathbf{H}\mathbf{x}_b\right] \tag{16}$$

where $\mathbf{x}_a$ is the analysis state, $\mathbf{x}_b$ is the prior forecast state, $\mathbf{B}$ is the background error covariance, $\mathbf{R}$ is the observation error covariance, $\mathbf{H}$ is the observation operator (maps the model state to the space of the observations), and $\mathbf{y}$ is the vector of observations. For NCODA, the operations of $\mathbf{B}\mathbf{H}^{\mathrm{T}}$ and $\mathbf{H}\mathbf{B}\mathbf{H}^{\mathrm{T}}$ are handled entirely by the covariance as an observation-to-model grid and observation-to-observation error covariance, respectively

$$\mathbf{x}_a = \mathbf{x}_b + \mathbf{P}_{om}(\mathbf{P}_{oo} + \mathbf{R})^{-1}\left[\mathbf{y} - \mathbf{H}\mathbf{x}_b\right] \tag{17}$$

where $\mathbf{P}_{om}$ is the background error covariance between the observations and model state and $\mathbf{P}_{oo}$ is the background error covariance between the observations themselves. In NCODA, the background error covariance is modeled by using a second-order autoregressive function for horizontal error correlation and a Gaussian vertical correlation multiplied by an estimate of the forecast error variance. The forecast error variance is computed from a climatology of ocean *in-situ* profiles from the GDEM v4 [34], which produces monthly 3-D error variance fields for the entire globe. This error is reduced in regions that are recently sampled by assimilated observations using an estimate of the analysis error variance (which NCODA produces). This error is grown back to climatology over a set timescale if the region is not sampled by observations in subsequent analysis cycles. Standard observation sources used in these experiments include satellite SST from the GOES 16, METOP, VIIRS, and ocean-bound ship observations and NOAA buoys; SSHA from JASON-3, Sentinel-3A, Sentinel-3B, and SARAL/AltiKa DP; and ocean temperature and salinity profiles from the ARGO program.

The Relocatable NCOM Ensemble Forecast System (RELO-EFS): The ocean modeling system RELO (RELOcatable NCOM) is used here to run the entire suite of ocean observation processing and assimilation (through NCODA), and modeling (through NCOM). RELO also has the capacity to run ensemble forecasts using the ensemble transform (ET) method [35], [36], [37]. At each analysis time (every 24 h in the work shown here), the RELO ET transforms perturbations in the ensemble forecast into new perturbations that have the analysis error variance as computed by NCODA. To do this, the forecast perturbations and analysis perturbations of the *n*-sized model state are defined as

$$\mathbf{Z}^f = \frac{1}{\sqrt{k-1}}\left[\mathbf{z}_1^f, \mathbf{z}_2^f, \ldots, \mathbf{z}_k^f\right]$$

$$\mathbf{Z}^a = \frac{1}{\sqrt{k-1}}\left[\mathbf{z}_1^a, \mathbf{z}_2^a, \ldots, \mathbf{z}_k^a\right] \tag{18}$$

where $\mathbf{Z}^f$ and $\mathbf{Z}^a$ are the set of forecast and analysis perturbations, respectively, for all k ensemble members. If we examine the ith ensemble member, the forecast and analysis perturbations can be defined as $\mathbf{z}_i^f = \mathbf{x}_i^f - \bar{\mathbf{x}}^f$ and $\mathbf{z}_i^a = \mathbf{x}_i^a - \hat{\mathbf{x}}^a$, where $\bar{\mathbf{x}}^f$ is the ensemble mean forecast state and $\hat{\mathbf{x}}^a$ is the analysis state given by NCODA (operating on the deterministic forecast state). The forecast and analysis $n \times n$ covariance matrices can, therefore, be approximated by

$$\mathbf{P}^f = \mathbf{Z}^f\mathbf{Z}^{f\mathrm{T}} \text{ and } \mathbf{P}^a = \mathbf{Z}^a\mathbf{Z}^{a\mathrm{T}}. \tag{19}$$

For a given set of forecast perturbations, the analysis perturbations can be obtained through what is called an "ensemble transformation" $\mathbf{T}$, such that $\mathbf{Z}^a$ can be defined as

$$\mathbf{Z}^a = \mathbf{Z}^f\mathbf{T}. \tag{20}$$

Now it is a matter of deriving the transformation matrix. NCODA produces the analysis error variance, which comprises the diagonal elements of $\mathbf{P}^a$. Given this, one can solve the following eigenvalue problem:

$$\mathbf{Z}^{f\mathrm{T}}\mathbf{P}_{\mathrm{diag}}^{a-1}\mathbf{Z}^f = C\mathbf{\Gamma}C^{-1} \tag{21}$$

where C contains the column orthonormal eigenvectors of $\mathbf{Z}^{f\mathrm{T}}\mathbf{P}_{\mathrm{diag}}^{a-1}\mathbf{Z}^f$ and $\mathbf{\Gamma}$ is a diagonal matrix containing the eigenvalues. The transformation matrix can now be constructed as $\mathbf{T} = C\mathbf{G}^{-1/2}$ where $\mathbf{G} = \mathrm{diag}(\lambda_1, \lambda_2, \lambda_3, \ldots, \lambda_{k\text{-}1}, \alpha)$; here, λ are the eigenvalues contained in $\mathbf{\Gamma}$ and α is a constant. Given this definition of $\mathbf{T}$, the new analysis perturbations can be derived as

$$\mathbf{Z}^a = \mathbf{Z}^f C\mathbf{G}^{-1/2}C^{\mathrm{T}}. \tag{22}$$

The new analysis perturbations derived in (22) are centered, i.e., the sum of all perturbations is zero.

For the experiments conducted here, the RELO-EFS is used to generate and propagate 50 ensemble members, each at 1-km resolution with 96-h forecasts for each analysis cycle. During the forecast period of each ensemble member, the atmospheric surface forcing (provided to NCOM from an offline atmospheric model) is also uniquely perturbed, thereby increasing the ensemble spread. Perturbations in the atmospheric forcing are derived by "time-shifting" the fields (stored by the atmospheric model and read-in by NCOM every 3 h). This time-shifting is done by linearly interpolating to some random point in-time between two of the three-hourly output fields provided by the atmospheric model [36], [37].

ACKNOWLEDGMENT

The authors would like to express appreciation to Dr. G. G. Gawarkiewicz and Dr. Y. T. Lin and the Woods Hole Oceanographic Institution for their willingness to support Portland State University participation in the 2021 NESBA experiment. The authors would also like to express appreciation for several key discussions with Dr. L. Stone of Metron Inc., dealing with the history and practice of computing and interpreting Navy cumulative probability of detection and related uncertainty metrics. Finally, the authors would like to thank the reviewers for taking

the time and effort necessary to review the manuscript and for their valuable comments and suggestions, which helped us improve the quality of the manuscript.

REFERENCES

[1] R. J. Urick, *Principles of Underwater Sound*, 3rd ed. New York, NY, USA: McGraw-Hill, 1983, ch. 6.7.

[2] I. Dyer, "Statistics of sound propagation in the ocean," *J. Acoust. Soc. Amer.*, vol. 48, no. 1B, pp. 337–345, 1970.

[3] J. A. Colosi, *Sound Propagation Through the Stochastic Ocean*. Cambridge, U.K.: Cambridge Univ. Press, 2016.

[4] E. S. Livingston, J. A. Goff, S. Finette, P. Abbot, J. F. Lynch, and W. S. Hodgkiss, "Guest editorial capturing uncertainty in the tactical ocean environment," *IEEE J. Ocean. Eng.*, vol. 31, no. 2, pp. 245–248, Apr. 2006.

[5] C. D. S. Tollefsen, "Predicting acoustic variability: Pragmatic considerations for selecting a stochastic or deterministic approach," *IEEE J. Ocean. Eng.*, vol. 46, no. 3, pp. 1045–1056, Jul. 2021.

[6] K. D. Heaney and H. Cox, "A tactical approach to environmental uncertainty and sensitivity," *IEEE J. Ocean Eng.*, vol. 31, no. 2, pp. 356–367, Apr. 2006.

[7] P. Abbot, I. Dyer, and C. Emerson, "Acoustic propagation uncertainty in the shallow East China Sea," *IEEE J. Ocean Eng.*, vol. 31, no. 2, pp. 368–383, Apr. 2006.

[8] R. J. Urick, *Ambient Noise in the Sea*. Los Altos, CA, USA: Peninsula, 1986.

[9] G. m. Wenz, "Acoustic ambient noise in the ocean: Spectra and sources," *J. Acoust. Soc. Amer.*, vol. 34, no. 12, pp. 1936–1956, 1962.

[10] L. Emery, M. Bradley, and T. Hall, "Database description (DBD) for the historical temporal shipping database variable resolution (HITS)," Version 4.0, Planning Syst., Inc., Slidell, LA, USA, Tech. Rep. TRS-301, 2001.

[11] W. K. Stevens, M. Siderius, M. Carrier, Y. T. Lin, and D. Wendeborn, "Ocean ensemble-enabled stochastic acoustic prediction with operational metrics: NESBA signals and noise experiment," *IEEE J Ocean. Eng.*, to be published, doi: 10.1109/JOE.2023.3267788.

[12] National Academy of Engineering, *Environmental Information for Naval Warfare*. Washington, DC, USA: Nat. Acad. Press, 2005. [Online]. Available: www.nap.edu

[13] Naval Studies Board, *Technology for the United States Navy and Marine Corps, 2000-2035: Becoming a 21st-Century Force: Volume 7: Undersea Warfare*. Washington, DC, USA: Nat. Acad. Press, 1997. [Online]. Available: www.nap.edu

[14] A. Washburn, "A multistatic sonobuoy theory," Nav. Postgraduate School, Monterey, CA, USA, Tech. Rep. NPS-OR-10-005, 2010.

[15] A. Washburn and M. Karatas, "Multistatic search theory," *Mil. Oper. Res. J.*, vol. 20/1, pp. 21–38, 2015.

[16] D. P. Kierstead and D. R. DelBalzo, "A genetic algorithm applied to planning search paths in complicated environments," *Mil. Oper. Res.*, vol. 8, no. 2, pp. 45–59, 2003.

[17] X. Zeng et al., "Use of observing system simulation experiments in the United States," *Bull. Amer. Meteorol. Soc.*, vol. 101, no. 8, pp. 1427–1438, Aug. 2020.

[18] *General Bathymetric Chart of the Ocean (GEBCO)*, International Hydrographic Organization (IHO). [Online]. Available: https://www.gebco.net

[19] C. H. Harrison and D. G. Simons, "Geoacoustic inversion of ambient noise: A simple method," *J. Acoust. Soc. Amer.*, vol. 112, pp. 1377–1389, 2002.

[20] M. D. Collins, "A split-step Padé solution for parabolic equation method," *J. Acoust. Soc. Amer.*, vol. 93, pp. 1736–1742, 1993.

[21] M. D. Collins, "Generalization of the split-step Padé solution," *J. Acoust. Soc. Amer.*, vol. 96, pp. 382–385, 1993.

[22] N. C. Makris, "The effect of saturated transmission scintillation on ocean acoustic intensity measurements," *J. Acoust. Soc. Amer.*, vol. 100, no. 2, pp. 769–783, Aug. 1996.

[23] B. O. Koopman, *Search and Screening, Operations Evaluation Group Report 56*, Washington, DC, USA: Office of the Chief of Naval Operations, 1946, ch. 3.

[24] D. H. Wagner, W. C. Mylander, and T. J. Sanders, *Naval Operations Analysis*, 3rd ed. Annapolis, MD, USA: Naval Inst. Press, 1999, ch. 5.

[25] E. W. Dijkstra, "A note on two problems in connexion with graphs," *Numerische Mathematik*, vol. 1, pp. 269–271, 1959.

[26] R. K. Ahuja, T. L. Magnanti, and J. B. Orlin, *Network Flows: Theory, Algorithms and Applications*. London, U.K.: Pearson, 1993.

[27] MATLAB, "Version R2022a update 1," MathWorks Inc., Natick, MA, USA, 2022.

[28] "Database descriptions for the generalized digital environmental model (GDEM-V) version 3.0 and 3.0.2 databases," OAML-DBD-72G (Rev.), Nav. Oceanographic Office, John C. Stennis Space Center, MS, USA, Jan. 2012.

[29] E. P. Chassignet et al., "The HYCOM (HYbrid Coordinate Ocean Model) data assimilative system," *J. Mar. Syst.*, vol. 65, no. 1–4, pp. 60–83, 2007.

[30] "Database description for bottom sediment type," Nav. Oceanographic Office, Acoust. Division, John C. Stennis Space Center, MS, USA, OAML-DBD-86, Approved for Public Release, Distribution is Unlimited, Sep. 2003.

[31] L. H. Kantha and C. A. Clayson, "On the effect of surface gravity waves on mixing in an oceanic mixed layer model," *Ocean Model.*, vol. 6, pp. 101–124, 2004.

[32] J. A. Cummings and O. m. Smedstad, "Variational data analysis for the global ocean," in *Data Assimilation for Atmospheric, Oceanic and Hydrologic Applications*, vol. II, S. K. Park and L. Xu, Eds., Berlin, Germany: Springer, 2013.

[33] T. F. Hogan et al., "The navy global environmental model," *Oceanography*, vol. 27, pp. 116–125, 2014.

[34] M. Carnes, R. W. Helber, C. N. Barron, and J. m. Dastugue, "Validation test report for GDEM4," Nav. Res. Lab., John C. Stennis Space Center, MS, USA, Tech. Rep. NRL/MR/7330-10-9271, 2010.

[35] C. H. Bishop and Z. Toth, "Ensemble transformation and adaptive observations," *J. Atmos. Sci.*, vol. 56, pp. 1748–1765, 1999.

[36] M. Wei, C. Rowley, P. Martin, C. Barron, and G. Jacobs, "The U.S. Navy's RELO ensemble prediction system and its performance in the Gulf of Mexico," *Quart. J. Roy. Meteorol. Soc.*, vol. 140, pp. 1129–1149, 2014.

[37] M. Wei et al., "The performance of the US Navy's RELO ensemble, NCOM, HYCOM during the period of GLAD at-sea experiment in the Gulf of Mexico," *Deep Sea Res. II, Topical Stud. Oceanogr.*, vol. 129, pp. 374–393, 2016.

William K. Stevens received the B.S. degree in mathematics from Northeastern University, Boston, MA, USA, in 1975, and the M.Sc. and Ph.D. degrees in applied mathematics from Brown University, Providence, RI, USA, in 1976 and 1979, respectively.

He is currently a part-time Adjunct Research Associate with Portland State University, Portland, OR, USA, and Senior Analyst with the Metron Inc., San Diego, CA, USA. He held a postdoctoral position with the Harvard-Smithsonian Center for Astrophysics from 1979 to 1980, was an Assistant Professor of mathematics with Northeastern University from 1980 to 1982, and held positions with the Center for Naval Analyses–Operations Evaluation Group and Daniel H. Wagner Associates from 1982 to 1985. He founded Metron's Simulation Sciences and High-Performance Computing Divisions in San Diego, CA (1989 and 1999). He was also the Founder and CEO of Applied Operations Research, San Diego, CA (2006–2015). His research interests include operations research, optimization, ocean acoustics, and decision support concept design and implementation.

Martin Siderius received the B.S. degree in physics from Western Washington University, Bellingham, WA, USA, in 1986, and the m.S. and Ph.D. degrees in electrical engineering from the University of Washington, Seattle, WA, USA, in 1992 and 1996, respectively.

From 1990 to 1996, he was a Research Assistant with the Applied Physics Laboratory, University of Washington. In 1996, he joined the Scientific Staff with the NATO Undersea Research Centre, La Spezia, Italy. From 2001 to 2004, he was a Senior Scientist with the Science Applications International Corporation and in 2004 cofounded HLS Research Inc., San Diego, CA, USA, and served as the Vice-President and a Principal Scientist. In 2008, he joined the faculty of the Department of Electrical and Computer Engineering, Portland State University, Portland, OR, USA, where he is currently a Professor. His research interests include underwater acoustic propagation and scattering, signal processing, ocean ambient noise, geoacoustic inversion, acoustic communications, and marine mammal acoustics.

Matthew J. Carrier received the B.S. degree in meteorology from Lyndon State College, Lyndonville, VT, USA, in 2002, and the M.S. and Ph.D. degrees in meteorology from Florida State University, Tallahassee, FL, USA, in 2004 and 2008, respectively.

He is currently a Research Oceanographer with the Ocean Sciences Division, U.S. Naval Research Laboratory, Stennis Space Center, MS, USA. His current research focuses on the variational data assimilation and its various applications, particularly as it pertains to indirect measurements of the ocean environment for navy ocean modeling.

Drew Wendeborn received the B.S. degree in mechanical engineering, in 2020, from Portland State University, Portland, OR, USA, where he is currently working toward the master's degree in electrical engineering.

He is a full-time Engineer with the Metron, Inc., Portland, OR, USA. From 2011 to 2019, he was in research and development for the airborne remote sensing company, Quantum Spatial. From 2020 to 2022, he was a Graduate Research Assistant with the Portland State University NEAR Lab and a Research Scientist Intern with Metron.